Brain-State-Dependent Modulation of Neuronal Firing and Membrane Potential Dynamics in the Somatosensory Thalamus during Natural Sleep

Nadia Urbain, Nicolas Fourcaud-Trocmé, Samuel Laheux, Paul A. Salin, Luc J Gentet

Brain state dependent modulation of neuronal firing and membrane potential dynamics in the somatosensory thalamus during natural sleep

Nadia Urbain [1 *], Nicolas Fourcaud-Trocmé [2], ***Samuel Laheux*** [1], Paul A. Salin [3], Luc J. Gentet [4]

[1] Physiopathology of sleep networks, [2] Coding in Memory and Olfaction, [3] Forgetting processes and Cortical dynamics, [4] Integrated Physiology of Brain Arousal Systems, Lyon Neuroscience Research Center, INSERM U1028-CNRS UMR5292, Université Claude-Bernard-Lyon 1, 69372 Lyon, France.

[*] Correspondence to: nadia.urbain@inserm.fr

**** Lead Contact: Nadia Urbain (nadia.urbain@inserm.fr)***

Running title: The sensory thalamus of sleeping mice

SUMMARY

The thalamus plays a central role in sleep rhythms in the mammalian brain yet, surprisingly little is known about its function and interaction with local cortical oscillations during NREM sleep (NREM). We investigated the neuronal correlates of cortical barrel activity in the two corresponding thalamic nuclei, the ventral posterior medial (VPM) and the posterior medial (Pom) nuclei, during natural NREM in mice. Our data reveal 1) distinct modulations of VPM and Pom activity throughout NREM episodes, 2) a thalamic nucleus-specific phase-locking to cortical slow and spindle waves, 3) cell-specific subthreshold spindle oscillations in VPM neurons that only partially overlap with cortical spindles, 4) that spindle features evolve throughout NREM episodes and vary according to the post-NREM state. Taken together, our results suggest that, during natural sleep, the barrel cortex exerts a leading role in the generation and transfer of slow rhythms to the somatosensory thalamus and reciprocally for spindle oscillations.

INTRODUCTION

Slow rhythms and spindle oscillations form the hallmarks of non-rapid eye movement sleep (NREM). Phase coupling between spindles, slow cortical oscillations and hippocampal ripples contributes to effective memory consolidation during sleep (Maingret et al., 2016; Latchoumane et al., 2017). However, despite the large interest for sleep and its markers, little is known about how the thalamus and the cortex interact during natural sleep. Most of our knowledge about membrane potential dynamics and nucleus-specific thalamic activity stems from *in vitro* slice and *in vivo* anesthetized animal studies (Steriade et al., 1993; McCormick and Bal, 1997). Ketamine-xylazine anesthesia, commonly used as a model system for sleep research, produces highly rhythmic and larger amplitude cortical slow waves compared to natural NREM (Chauvette et al., 2011). It essentially locks the variable slow-wave rhythms to a very narrow frequency range (Crunelli and Hughes, 2010), imposing synchrony and homogeneity on cortical targets. ***One study to date investigated, in cats, single-unit membrane potential dynamics during sleep (Hirsch et al., 1983).*** To uncover the functioning of the thalamocortical loop in naturally-sleeping animals, simultaneous measurements of thalamic and local cortical activity are required. Focusing on the mouse somatosensory system, we find a highly dynamic interplay between thalamic membrane potential dynamics and neuronal firing activity in the ventral posterior medial nucleus (VPM) and the posterior medial group (Pom), and local oscillations in barrel cortex during NREM.

RESULTS

We performed extra- and intra-cellular recordings of thalamic relay cells combined with S1 local field potential (S1-LFP) while simultaneously measuring the electroencephalogram (EEG) and the electromyogram (EMG) (Figure 1). These recordings allowed us to investigate the dynamics of thalamic subthreshold and spiking activity coupled with cortical oscillations across episodes of NREM in non-anesthetized mice.

Dynamic modulation of S1-LFP oscillations across NREM episodes

NREM was clearly distinguished by high-voltage *slow* waves (0.1 - 1.5 Hz) in both EEG and S1-LFP frequency spectra, prominent spindle (7 - 18 Hz) oscillations on S1-LFP and a weak EMG activity (Figures 1C, 2 A-C, S1 A-B,D). Since we observed that NREM dynamics evolve over the time course of a sleep episode, NREM episodes were divided in two parts of equal duration (Figure 2). In order to determine whether those dynamics differed according to future transitions from NREM to wake (WK) or REM sleep (REM), we further separated NREM episodes followed by WK (WK-f, n= 102) from those followed by REM (REM-f: n= 33) (Table S1).

The second half of NREM, whether followed by WK or REM, was characterized by a lower average spindle frequency (Figure 2 A-D; WK-f: 12.6 ± 0.1 vs 12.3 ± 0.1 Hz, $p< 0.05$; REM-f: 12.6 ± 0.1 vs 11.7 ± 0.1 Hz, $p< 0.001$) and a higher duration of cycles within spindles (WK-f: 84 ± 1 vs

86 ± 1 ms, p< 0.05; REM-f: 84 ± 1 vs 90 ± 1 ms, p< 0.001). In contrast, the number of cycles per spindle increased when NREM was followed by WK (5.7 ± 0.2 vs 6.4 ± 0.2 cycles/spindle, p< 0.001), but decreased when NREM was followed by REM (6.2 ± 0.3 vs 5.5 ± 0.2 cycles/spindle, p< 0.05). We observed significant changes in spindle features in the second part of NREM episodes followed by WK (Figure 2D): the spindle density increased (ratio of spindles duration per NREM episode duration = 0.25 ± 0.01 vs 0.33 ± 0.01, p< 0.001), spindles exhibited longer average durations (0.51 ± 0.01 vs 0.59 ± 0.02 s, p< 0.001) and occurred more frequently (0.48 ± 0.02 vs 0.56 ± 0.02 Hz, p< 0.01). In contrast, we did not observe any significant differences in *theta*/*delta* ratios calculated on second versus first half of NREM episodes, indicating that both halves still display basic features of NREM whether they are followed by WK or REM (Figure S1C).

Spindles appeared nested on cortical slow wave oscillations (Figure 2B). We therefore analyzed the distribution of spindles along the slow oscillation cycle. We found that spindle oscillations started near the trough of deep layer S1-LFP slow wave, corresponding to cortical Up-state when cortical neurons are active (Destexhe et al., 2007) (+ 8 ± 2°, n= 162 NREM episodes; 0°: trough). The average phase of spindle oscillations at both onset and peak amplitude relative to the slow wave trough occurred significantly earlier in the second versus first half of NREM (Figure 2E; spindle onset: NREM second half 0 ± 3° vs first half +20 ± 3°, p<0.001; spindle maximal amplitude: NREM second half +50 ± 3° vs first half +67 ± 3°, p<0.001).

Together, our data show that S1-LFP is highly dynamic throughout the time course of a NREM episode. Differences in spindle features occurring in the second half of NREM might reflect specific cortical and subcortical activation, initiated as a preparatory and/or complementary mechanism to the later processing occurring during the subsequent WK or REM period. Therefore, we next investigated the activity of thalamic cells in relation to spindles and slow wave activity.

Tight coupling between thalamic relay cells activity and S1-LFP oscillations during NREM

Forty-three VPM and 22 Pom cells were recorded extracellularly simultaneously with S1-LFP during NREM (Figure 3, Tables S1, S2). The vast majority of all spikes in both VPM and Pom cells occurred in bursts during NREM (VPM: 81 ± 2 %; Pom: 71 ± 3 %; figures 1C-D, 3A-C, S2A). These high frequency bursts were characterized by a mean interspike interval (ISI) of 2.7 ± 0.1 ms for VPM and 3.3 ± 0.1 ms for Pom cells and a mean number of spikes per burst of 3.7 ± 0.1 for VPM and 3.2 ± 0.1 for Pom cells. Within bursts, ISI durations increased, while spike amplitudes decreased, for each subsequent spike (Figure S2C,D), as previously described for thalamic relay cells (Domich at al., 1986).

Next, we analyzed the firing dynamics of thalamic cells through NREM episodes. Spike and burst rates of VPM cells increased significantly in the second half of NREM, whether it was followed by WK or REM (Figure 3C; WK-f: 6.84 ± 0.90 vs 8.35 ± 0.75 spikes / s, p< 0.01 and 1.38 ± 0.13 vs 1.87 ± 0.13 bursts / s, p< 0.001, n = 35 cells; REM-f: 6.28 ± 0.71 vs 8.62 ± 0.83 spikes / s, p< 0.001 and 1.42 ± 0.14 vs 1.96 ± 0.18 bursts / s, p< 0.01, n= 13 cells). In contrast, Pom cell firing

and burst rates remained unchanged in both NREM halves (WK-f: 3.78 ± 0.27 vs 4.16 ± 0.28 spikes / s and 0.75 ± 0.08 vs 0.91 ± 0.09 burst / s, n= 16 cells; REM-f: 4.59 ± 0.57 vs 5.08 ± 0.81 spikes / s and 1.07 ± 0.12 vs 1.12 ± 0.21 bursts / s, n= 8 cells).

We further examined the spike timing of thalamic cells relative to spindle cycles and found that 73% of VPM cells (n= 30/41) and 67% of Pom cells (n= 12/18) exhibited spiking at specific phases ($p< 0.01$, Rayleigh test) (Figure 3B,D). At a population level, VPM cells spiked preferentially 84 ± 7° before the spindle trough ($p< 0.001$; n= 30 modulated cells; Figure 3D), while no significant phase preference was observed in Pom cells ($p= 0.02$; n= 12 modulated cells).

Similarly, the distribution of thalamic spikes on S1-LFP slow waves was assessed for 38 VPM and 19 Pom cells (Figure 3E): 84% of VPM (n= 32/38) and 63% of Pom cells (n= 12/19) exhibited spike firing at specific phases on the cortical slow wave cycle ($p< 0.01$, Rayleigh test), preferentially occurring after the trough. At a population level, VPM cells spiked preferentially 80 ± 5° after the slow wave trough ($p< 0.001$; n= 32 modulated cells), while a larger disparity in preferred angles for spikes firing on slow waves was observed among the modulated Pom cells ($p= 0.01$; n= 12 ; average preferred phase: 68 ± 18° after slow wave trough).

We next computed S1-LFP spike-triggered averages (STA) to investigate the impact of thalamic spikes at the level of the barrel cortex during NREM (Figure 3F). The population STA calculated for VPM cells (n= 32) revealed a cortical peak lagging at ~15 ms after thalamic VPM spikes. In comparison, the population STA of S1-LFP computed for Pom spikes (n= 9 cells) did not display any distinguishable peak. We did not observe any phase difference in VPM spikes distribution on cortical slow and spindles waves, nor for STA, between the first and second halves of NREM episodes, whether followed by WK or REM sleep. Spike timing in thalamic cells relative to cortical activity appeared therefore well preserved throughout NREM.

Optogenetic stimulation of S1 cortex evoked spindle-like activity

In S1-LFP, we often detected spontaneous *delta* waves followed by spindles during NREM, as previously described in other cortical areas (Contreras and Steriade, 1996; Amzica and Steriade, 1998; Vyazovskiy et al., 2009). Such events correspond to a cortical Down-state, during which cortical neurons stop firing (Contreras and Steriade, 1995; Maingret et al., 2016). In order to examine whether such a cortical silencing is reflected in the firing of thalamic cells, we computed peristimulus time histograms (PSTHs) of spikes aligned to *delta* wave onset for VPM and Pom neurons (Figure 4A). A significant decrease in both VPM and Pom discharges appeared within the 0-100ms after the *delta* event onset (VPM: 0-100 ms, 3.1 ± 0.9 Hz vs baseline 7.0 ± 0.8 Hz, $p< 0.001$, n= 35; Pom: 0-100 ms, 2.3 ± 1.6 Hz vs baseline 5.2 ± 1.5 Hz, $p< 0.01$, n= 19). In VPM cells only, this decrease in spike firing was followed by a significant rebound of activity (250-500 ms, 10.6 ± 0.9 Hz vs baseline 7.0 ± 0.8 Hz, $p< 0.01$; figure 4B), concomitant with the advent of spindle-band activity in S1-LFP (top trace on figure 4A).

To gain insight into the functional contribution of S1 cortex to thalamic activity, we performed optogenetic stimulation of S1 pyramidal neurons expressing ChR2 in Thy1-ChR2 transgenic mice (Matyas et al., 2010). Photo-activation of S1 cortical surface resulted in a sharp downward deflection in the LFP (peak latency: 13.2 ± 0.2 ms, n= 13; Figure 4C), followed by a *delta* wave of 132.6 ± 1.9 ms duration (peak latency: 89.0 ± 4.1 ms). In addition, wavelet time-frequency analysis revealed spindle-like activity in S1-LFP (~ 15 Hz) lasting 250 ms from 100 to 350 ms after light onset (Figure 4C, top).

At the thalamic level, photo-activation of S1 cortex evoked a potent decrease in VPM neuronal firing (20-100 ms, 1.5 ± 0.5 Hz vs baseline 6.8 ± 1.0 Hz, $p< 0.01$, n= 13; Figure 4C-D); VPM cells recovered their ability to fire after the peak of the *delta* event. This rebound of activity, in the 100-400 ms range after light onset, was characterized by a higher probability of burst occurrence compared to the baseline period (100-400 ms period, 64.0 ± 0.1 % vs baseline, 18.1 ± 0.1 %, $p< 0.01$). Thus, activation of S1 pyramidal cells evoked a thalamic silencing followed by rebound bursts in VPM cells, mimicking the thalamic ISIs distribution observed during NREM (Figure 3C, S2A).

We further performed intracellular recordings of VPM and Pom cells during NREM and analyzed their membrane potential dynamics at the onset of *delta* waves observed in S1-LFP (Figure 4E). Our result showed that the membrane potential (Vm) of both VPM and Pom thalamic cells exhibited a long-lasting hyperpolarization which started shortly after the onset of cortical *delta* waves (0-100 ms period: VPM, -0.8 ± 0.2 mV, $p< 0.01$, n= 10; Pom, -1.2 ± 0.5 mV, $p< 0.05$, n= 5; Figure 4E,F).

Coupling between S1-LFP activity and membrane potential dynamics of thalamic cells during NREM

Our intracellular recordings also revealed that Vm in both VPM and Pom cells were more hyperpolarized in NREM than in quiet wakefulness (i.e. the most hyperpolarized state described while the mice are awake; VPM: -67.5 ± 2.0 mV vs -62.5 ± 2.2 mV, $p< 0.01$, n= 9; Pom: -65.8 ± 1.2 mV vs -62.2 ± 1.7 mV, $p< 0.05$, n= 5; Figure 5A-C). We next examined the dynamics of Vm over the time course of NREM episodes and found a further significant increase in Vm hyperpolarization during the second half of NREM in VPM cells (Figure 5C; NREM second half -66.5 ± 3.0mV vs NREM first half -65.7 ± 2.9 mV, n= 6; Table S1), which might contribute to the observed increase in VPM burst firing during this period (Figures 1C, 3C). Pom cells also tended to hyperpolarize more in the second part of NREM (-65.0 ± 1.7 mV in second part vs -64.0 ± 1.6 mV in first part, n= 3; figure 5C).

Both VPM and Pom cells exhibited Vm slow oscillations (Peak-to-peak Vm: VPM, 3.9 ± 0.9 mV, range: 1.5 - 10.5 mV, 0.52 ± 0.03 Hz, n= 10; Pom, 4.8 ± 1.0 mV, range: 2.6 - 8.4 mV, 0.59 ± 0.05 Hz, n= 5) (Figures 5D, S3). We observed that firing probability was significantly lowest on Vm slow oscillations' trough, i.e. most hyperpolarized Vm, in VPM neurons (Figure 5E, Rayleigh test,

p≤0.01, n= 6 VPM and 2 Pom cells). Remarkably, 4 out of 10 VPM cells and 3 out of 5 Pom cells did not fire any action potential during NREM.

The temporal relationship between the thalamic membrane potential and cortical waves was investigated by computing averages of thalamic Vm across cortical slow waves collected during NREM (Figures 5F). We found that the time course of thalamic-Vm was significantly modulated on S1-LFP slow waves, relative to shuffled data, for 8 out of 10 VPM cells and 3 out of 5 Pom cells ($p < 0.01$; figure S4; see STAR Methods). We observed that thalamic-Vm was more hyperpolarized on the cortical Up-state, and started to depolarize on the falling phase of the cortical Up-state.

We observed Vm oscillations in the spindle frequency range in a subset of VPM cells (n= 4 out of 10), but not in Pom neurons (Figure 6A). During NREM, we found that Vm spindle oscillations in VPM neurons were concomitant with cortical spindles over 66% of the total time duration of S1-LFP spindles. Reciprocally, the degree of overlap between S1-LFP and thalamic spindles was significantly lower when reported over the total duration of thalamic Vm spindles (51%; $p < 0.05$) (Figure 6B). Average cross-correlation of Vm with S1-LFP was indeed significantly lower during natural NREM than under anesthesia (Figure S6E). To reveal any dynamic modulation of the level of correlation between the two signals across NREM, we then computed cross-correlograms on 400ms sliding windows. Cross-correlation indices between thalamic Vm and S1-LFP (see STAR Methods) were highly variable during NREM but were significantly higher during periods when either thalamic Vm, cortical LFP, or both, exhibited spindle oscillations than during periods without spindles in any of the two signals (Figure 6C). Therefore, unlike in the anesthetized animal (Contreras and Steriade, 1996; Bonjean et al., 2011), VPM-Vm and S1-LFP spindle oscillations frequently occurred simultaneously but were not strictly concomitant on longer time scales during natural sleep.

Synaptic activity in thalamic cells during NREM

Since the thalamus is thought to play a major role in the maintenance of sleep rhythms, we expected to observe a wealth of subthreshold synaptic activity in our intracellular recordings. Surprisingly, the background synaptic activity was sufficiently low that we could identify two populations of EPSPs in both VPM and Pom neurons, as previously described (Urbain et al., 2015). Fast-rising EPSPs represented the vast majority of excitatory events (VPM: 92.4 ± 2.4 %, n= 9; Pom: 96.7 ± 1.1 %, n= 5). Slow-rising EPSPs were rare during NREM both in VPM and Pom cells (VPM: 0.34 ± 0.07 Hz, n= 9 and Pom: 0.62 ± 0.39 Hz, n= 5; Figure 7C). Given the low rate of slow-rising EPSPs recorded in both nuclei during NREM, only fast-rising EPSPs were analyzed. During NREM, Pom cells exhibited a significantly higher EPSP rate (16.5 ± 4.3 Hz, n= 5) than VPM cells (6.2 ± 1.7 Hz, n= 10) (Figure 7C). Peak EPSP amplitudes were similar between the two nuclei (VPM: 3.4 ± 0.7 mV, n= 10; Pom: 2.6 ± 0.5 mV, n= 5; Figure 7D). Interestingly, half of these EPSPs occurred during spindles in Pom cells against one fourth in VPM cells (EPSPs on spindles / total EPSPs, Pom: 0.51 ± 0.05 and VPM: 0.26 ± 0.04). Fast-rising EPSPs occurrence was not

significantly modulated during cortical spindle activity in any VPM cells (p> 0.13, n= 9 cells), and in only 2 out of 5 Pom cells (p≤ 0.01) (Figures 7E). At the population level, EPSPs did not display any preferred phase on cortical slow wave in either VPM or Pom neurons (VPM, p= 0.35, n= 9; p= 0.16 for the n= 5 modulated cells; Pom, p= 0.40, n= 5 cells) (Figure 7F). Yet, fast-rising EPSPs occurrence was significantly modulated by cortical slow waves in 56% VPM (n= 5/9) and 40% Pom (n= 2/5) cells (p< 0.01, Rayleigh test; figure S5).

Membrane potential dynamics of VPM cells during NREM compared to anesthesia

In order to compare our data in naturally-sleeping mice with recordings obtained under anesthesia, we performed intracellular recordings of VPM cells under ketamine-xylazine (KX, n= 12 cells, 10 mice; figure S6). Of particular interest, we observed that Vm at rest calculated for cells recorded under KX was significantly more depolarized than resting Vm calculated for cells recorded in sleeping mice (p< 0.05; KX: -61.0 ± 2.4mV; NREM, -68.5 ± 2.0 mV; Figure S6C). No significant difference in neuronal firing rate was observed at rest between the two states (Figure S6D). The grand average of cross-correlograms between S1-LFP spindles and VPM-Vm displays, a clear peak centered at 18 ms both during NREM and under anesthesia, but a weaker peak correlation coefficient in NREM compared to KX (Figure S6E). Our data therefore suggests that the level of thalamo-cortical synchronization between Vm and S1-LFP is globally lower in sleeping mice than in anesthetized animals.

DISCUSSION

The interplay linking thalamic and cortical activity has been extensively studied *in vitro* or under anesthesia and has been characterized by a tight correlation between cortical oscillatory activity and thalamic firing patterns (Steriade et al., 1993; McCormick and Bal, 1997). However, mechanistic understanding of what drives action potential firing *in vivo* requires intracellular recordings ***and so far one study has been performed in the thalamus of naturally sleeping cats (Hirsch et al., 1983).*** By applying cross-correlations together with phase and time-frequency analysis to extra- and intracellular recordings performed in thalamic sensory nuclei concomitantly with cortical LFP recordings, we describe a more dynamic, time-varying interplay between thalamic neuronal activity in the VPM and Pom and their corresponding barrel somatosensory cortex during natural sleep in mice.

In a previous paper, we showed that neuronal firing and membrane potentials of VPM and Pom cells were dynamically related to a variety of cortical and behavioral states in awake mice (Urbain et al., 2015). In the present study, we similarly observed that NREM is a dynamic state that could be separated into two distinct halves. While Vm hyperpolarization in both VPM and Pom neurons was a hallmark of entire NREM episodes, it further increased in the second half of NREM episodes in VPM neurons and might contribute to the observed increase in VPM burst firing during this period. In parallel, at the level of the cortex, we observed larger spindle rates and densities

ahead of awakening. Spike timing in thalamic cells relative to cortical oscillations appeared however well preserved throughout NREM, with thalamic spikes occurring preferentially before the trough of the cortical spindle wave but after the trough of the cortical slow wave. While the membrane potential oscillations of thalamic cells were shown to be phase-locked with cortical slow-waves in anesthetized animals (Contreras and Steriade, 1996; Sheroziya and Timofeev, 2014; Groh et al., 2014), we observed a wealth of subthreshold thalamic activity reflecting, even though not strictly correlated to, the cortical versatility during this brain state.

An intriguing finding of the present study is that, despite its fragmented sleep pattern, cortical and thalamic activity in mice is highly dynamic over the time course of NREM episodes, with spindle density increasing in the second half of NREM episodes. We further show that most spindle features were differentially modulated throughout the time course of a NREM episode depending on the state following sleep (REM sleep or WK; Figure 2), indicating that these spindle properties may embed predictive information about the animal's future vigilance state. These differences in spindle features might reflect specific subcortico-cortical activity taking place in the second half of NREM as preparatory processing for what will lately occur during the REM period. Which subcortical mechanisms might account for these observed differences? Spindles are generated through a rhythmic interaction of excitatory thalamocortical neurons and inhibitory reticular thalamic cells (NRT), involving both the intrinsic membrane properties of these cells and their anatomical interconnections, that in turn entrains cortical activity (Steriade et al., 1993; McCormick and Bal, 1997). The 7 - 18 Hz spindle frequency reflects the property of NRT cells to generate rhythmic burst at this frequency range (Bal and McCormick, 1993). A currently held hypothesis is that strong, facilitating and synchronized NRT neurons bursting promotes slower thalamocortical oscillations (Beenhakker and Huguenard; 2009). Since VPM neurons excite NRT neurons, enhanced VPM activity may contribute to NRT hyperexcitability (Pinault et al., 1997; Gentet and Ulrich, 2003). We observed a distinct modulation of VPM activity across NREM episodes, with VPM neurons exhibiting an increase in discharge rate and more robust bursts in the second half of NREM. Such a strengthening of VPM bursting activity in the late part of NREM might therefore induce an increase in excitation onto NRT neurons and contribute to the shift from fast cortical spindles to slower but more robust cortical spindles at the level of mouse barrel cortex.

Our data further uncovered a preferential firing of VPM and Pom cells on the rising phase of the cortical spindle cycles during NREM (Figure 3D). However, in line with previous findings showing that thalamocortical projections from VPM, rather than Pom, are efficient transmitters of information to S1 cortex (Bruno and Sakmann, 2006; Viaene et al., 2011a, 2011c; Mease et al, 2016a; but see Audette et al., 2018), the impact of a single VPM spike on S1-LFP was more pronounced than that of a Pom neuron (Figure 3F). Hence, our findings corroborate the view that thalamic spikes (especially from VPM cells, i.e. first order thalamic nucleus) are involved in spreading spindles initiated in the thalamus to cortex during NREM (Halassa et al., 2011).

Consistent with previous reports in other cortical areas (Contreras and Steriade, 1996; Amzica and Steriade, 1998; Vyazovskiy et al., 2009), we observed that spindles often followed a *delta* wave in S1-LFP (Figure 4), suggesting that the fine temporal relation between spindles and *delta* waves is instrumental in shaping communication between neocortex and thalamus. Interestingly, *delta* waves triggered by cortical stimulation were also followed by cortical spindles, associated with rebound burst spiking activity in VPM cells, reminiscent of the triggered "spindling" activity described by Contreras and Steriade (1996) in the motor cortical area and the corresponding cells in the ventrolateral thalamic nucleus. *Delta* waves were shown to reflect the Down-states of the slow oscillation, when cortical neurons stop firing (Contreras and Steriade, 1995; Maingret et al., 2016). In the present study, we further show that suppression of firing activity also occur in thalamic cells during spontaneous or evoked cortical *delta* waves, likely through hyperpolarization of their membrane potential (Figure 4). Previous data in anesthetized animals suggest that this thalamic hyperpolarization is essentially a period of disfacilitation (absence of synaptic activities) with an additional hyperpolarization likely mediated by the activation of NRT cells (Contreras et al. 1996). The depth-negative sharp LFP deflection, which followed the delta wave, was shown to reflect the onset of the depolarizing phase of the slow cortical oscillation and the excitation of corticofugal neurons, and to powerfully drive NRT neurons (Contreras and Steriade, 1995). This excitation of GABAergic NRT cells may thus explain the prolonged hyperpolarizations that we observed in VPM and Pom cells on cortical Up-state (Figure 5D,F).

Superimposed on this Vm hyperpolarization, we observed Vm oscillations in the spindle frequency range in a subset of VPM cells. However, the temporal overlap between periods of single-neuron membrane potentials 7-18 Hz oscillations and S1-LFP cortical spindles was not strictly coincidental, contrary to what had been observed in anesthetized animals (Contreras and Steriade, 1996; Bonjean et al., 2011). Sliding-window cross-correlation analysis of both Vm VPM neuron and S1-LFP signals further uncovered a highly-dynamic modulation of their spatiotemporal coherence, with cross-correlation peaks occurring mainly when both signals were engaged in spindle-like oscillatory activity (Figure 6C). Decortication similarly leads to a weakening of correlation between thalamic and cortical spindle sequences (Contreras et al., 1997). Thus, we speculate, that the massive corticothalamic feedback loop responsible for highly synchronized thalamocortical spindle sequence initiation and efficient spread back to the cortex under anesthesia is dramatically weakened under conditions of natural sleep. In turn, NRT neurons may only initiate local spindle-like activity with one or few thalamic relay cells. This circuit configuration may allow for better fine-tuning of sensory inputs at the thalamic level during natural sleep than under anesthesia, indeed sustained spindle activity was shown to elevate arousal threshold (Wimmer et al., 2012).

Temporal firing of thalamic cells on cortical slow waves was demonstrated to differ between thalamic nuclei (Ushimaru et al., 2012; Gent et al., 2018). We found that both VPM and Pom cells fire spikes preferentially after the trough of the S1-LFP slow waves (Figure 3E), although with a

larger disparity of preferred phases among modulated Pom cells, in agreement with previous studies in anesthetized rats (Slézia et al., 2011). Interestingly, the delay we found is broadly consistent with recent findings in human showing a delay of roughly ¼ cycle from cortical Down peak to thalamic Down peak (Mak-McCully et al., 2017). The highest probability for firing of VPM and Pom cells after the peak of cortical slow waves is in accordance with our observations that S1-LFP spindles are synchronized with the peak of the Up-state, and not before the peak in contrast with human and cat EEG (Mölle et al., 2002). This indicates that the slow activity observed during NREM may be generated at the level of neocortex, rather than sensory thalamus (David et al., 2013; Lemieux et al., 2014). Higher jitter for Pom spike firing on S1 slow waves could be related to their connectivity patterns. While higher-order Pom cells receive “driver” synaptic inputs emanating from layer 5 cortical pyramidal cells, these synapses display pronounced short-term depression (Hoogland et al., 1991; Bourassa et al., 1995; Reichova and Sherman, 2004; Groh et al, 2008, 2014; Mease et al., 2016b). Strong inhibitory action exerted by synaptic inputs from the zona incerta and the anterior pretectum (Barthó et al., 2002; Bokor et al., 2005; Lavallée et al, 2005) may further contribute to impeding the efficient transmission of cortical inputs from S1 to Pom cells and broadening their spike distribution on cortical slow waves during NREM. Using intracellular recordings, we revealed that firing rate of thalamic cells increases with thalamic Vm depolarization (Figure 5E) which begins on the falling phase of cortical Up-states (Figure 5F). Such an increased probability for thalamic cells to fire spikes after the peak of Vm hyperpolarization rather than near the peak of Vm depolarization can be explained by the hyperpolarization-induced de-inactivation of the low-threshold calcium current in those neurons. Excitatory inputs on thalamic cells can then directly drive regenerative calcium spikes that can trigger bursts of action potentials. We indeed observed a higher probability for EPSPs to occur in VPM cells preferentially on the falling phase of cortical Up-states (Figure 7F).

Finally, intracellular recordings of thalamic neurons revealed that around half of VPM and Pom cells are silent during NREM. Interestingly, all silent Pom neurons in our dataset fired spikes during wakefulness (data not shown). It will be interesting to further probe whether NREM-silent VPM neurons can discharge during specific brain states or whether they belong to a pool of redundant cells with different intrinsic cellular properties (Epzstein et al., 2011). We could further show that the Vm of thalamic neurons was hyperpolarized by ~ 5mV after sleep onset (Figure 5A,B), as previously observed in sleeping cats (Hirsch et al., 1983). Similarly, we observed fewer fast-rising large amplitude EPSPs in VPM cells compared to Pom neurons during NREM, as previously observed in awake mice (Urbain et al., 2015). However, NREM was characterized by surprisingly low rates of occurrence of slow-rising EPSPs in both VPM and Pom neurons (<0.4 Hz), far less than was observed during wakefulness (Urbain et al., 2015). Since slow-rising EPSPs are thought to emanate from the modulatory inputs of S1-Layer 6 (Reichova and Sherman, 2004), our results therefore suggest a weaker impact of direct inputs coming from S1-Layer 6 onto thalamic cells during NREM in contrast with wakefulness (Hirai et al., 2017). However, our data do

not rule out the possibility that slow-rising EPSPs in Pom and VPM cells may be shunted by GABAergic inputs from the NRT (Cox et al., 1996; Pinault and Deschênes, 1998) or, for Pom cells, from the anterior pretectal nucleus (Bokor et al., 2005) and the zona incerta (Barthó et al., 2002). In the future, it will be important to examine the neuronal activity occurring in these brain structures during NREM.

In anesthetized rodents, it was shown that fast-rising EPSPs are rhythmically coupled to the cortical slow oscillation in Pom, but not VPM, cells (Groh et al, 2014; Sheroziya and Timofeev, 2014). In contrast, we observed that fast-rising EPSPs occurred at a specific phase of the S1-LFP slow wave in less than half of Pom cells (40%), and over half of VPM cells (56%) during NREM (Figures 7F, S6). The differences between our results and previous studies performed in anesthetized animals can be explained by a more pronounced rhythmicity and amplitude of slow oscillations under ketamine-xylazine (KX) anesthesia compared with oscillations recorded during natural NREM (Chauvette et al., 2011). By locking high amplitude slow waves to a very narrow frequency range (Amzica and Steriade, 1998; Crunelli and Hughes, 2010; Slézia et al., 2011), KX may potently and synchronously drive cortical outputs leading to stronger rhythmic barrages of fast-rising EPSPs impinging onto Pom neurons. EPSPs recorded under KX occurred during the cortical Up-states when cortical neurons are active, suggesting a cortical origin for these EPSPs (Groh et al., 2014). On the other hand, in NREM, we observed in half of the VPM cells that fast-rising EPSPs occurrence was modulated by S1-LFP slow waves, in contrast to previous studies under anesthesia (Groh et al, 2014; Sheroziya and Timofeev, 2014). One explanation might be that the strengthening of cortical excitatory outputs observed under KX anesthesia may increase membrane potential shunting via activation of inhibitory NRT neurons innervating VPM cells (Contreras et al., 1996; Pinault and Deschênes, 1998). Indeed, while large IPSPs phase-locked on cortical slow wave have been described in VPM neurons under anesthesia (Contreras and Steriade, 1996; Groh et al, 2014; Sheroziya and Timofeev, 2014), we rarely observed them in NREM. Such IPSPs may contribute to the dampening of excitatory synaptic activity in VPM cells under anesthesia, which could be then revealed by recordings performed in naturally sleeping animals exhibiting a highly dynamic and variable cortical activity.

Taken together our data uncovered a highly diverse thalamic activity both in VPM and Pom nuclei that reflects the fluctuating cortical LFP recorded in S1 during NREM. Simultaneous LFP recordings from distinct cortical regions showed that slow waves occur more synchronously in different areas during KX anesthesia than in NREM (Chauvette et al., 2011). Therefore natural sleep might segregate cortical areas, while KX anesthesia appears as a more homogeneous brain state. Although the use of anesthetics has greatly facilitated investigations of the cellular correlates of the slow oscillation, such anesthetics impose an overall rhythm at particular frequencies to cortical cells (Crunelly and Hugues, 2010). Our results suggest that a weaker correlation between Pom and S1-LFP activity prevails in NREM, but uncovers the presence of excitatory synaptic inputs coupled with cortical spindle and slow waves in VPM neurons. ***The present data therefore***

sheds light on the role of the thalamocortical loop in the generation and entrainment of slow rhythms and spindle oscillations which form the hallmarks of NREM in mammals.

ACKNOWLEDGMENTS

We warmly thank C. Petersen for the funding and hosting of experiments in Lausanne (EPFL, Switzerland), as well as the EPFL Faculty of Life Science Workshop for help with instrumentation. ***We thank P.A. Libourel for technical assistance***. We are grateful to D. Pinault, T. Bal, R. Lambert and N. Leresche for critical reading of the manuscript. This work was funded by a Marie-Curie Re-integration Grant (N.U.), ANR PARADOX (ANR-17-CE16-0024) (N.U., P.S. and L.G.) and FLAG-ERA JTC 2015 project CANON (co-financed by ANR) (L.G.).

AUTHOR CONTRIBUTIONS

N.U. designed the project and performed the experiments. N.U., N. F.-T., ***S.L.***, P.S. and L.G. analyzed the data. N.U. and L.G. wrote the manuscript. P.S. and N. F.-T. commented on the manuscript.

DECLARATION OF INTERESTS

The authors declare no competing interests.

SUPPLEMENTAL INFORMATION

Supplemental information includes 6 figures and 2 tables.

REFERENCES

Amzica, F., and Steriade, M. (1998). Cellular substrates and laminar profile of sleep K-complex. Neuroscience. *82*, 671-686.

Andrillon T., Nir Y., Staba R.J., Ferrarelli F., Cirelli C., Tononi G., and Fried I. (2011) Sleep spindles in humans: insights from intracranial EEG and unit recordings. J. Neurosci. *31*, 17821-17834.

Audette, N.J., Urban-Ciecko, J., Matsushita, M., and Barth, A.L. (2018). POm Thalamocortical Input Drives Layer-Specific Microcircuits in Somatosensory Cortex. Cereb Cortex. *28*, 1312-28.

Bal, T., and McCormick, D.A. (1993). Mechanisms of oscillatory activity in guinea-pig nucleus reticularis thalami in vitro: a mammalian pacemaker. J. Physiol. *468*, 669-691.

Barthó, P., Freund, T.F., and Acsády, L. (2002). Selective GABAergic innervation of thalamic nuclei from zona incerta. Eur. J. Neurosci. *16*, 999-1014.

Beenhakkerand, M.P., and Huguenard, J.R. (2009) Neurons that fire together also conspire together: is normal sleep circuitry hijacked to generate epilepsy? Neuron *62*, 612-632.

Bokor, H., Frère, S.G., Eyre, M.D., Slézia, A., Ulbert, I., Lüthi, A., and Acsády, L. (2005). Selective GABAergic control of higher-order thalamic relays. Neuron *45*, 929-940.

Bonjean, M., Baker, T., Lemieux, M., Timofeev, I., Sejnowski, T., and Bazhenov, M. (2011). Corticothalamic feedback controls sleep spindle duration in vivo. J. Neurosci., *31*, 9124-9134.

Bourassa, J., Pinault, D., and Deschênes, M. (1995). Corticothalamic projections from the cortical barrel field to the somatosensory thalamus in rats: a single-fibre study using biocytin as an anterograde tracer. Eur. J. Neurosci. *7*, 19-30.

Bruno, R.M. and Sakmann, B. (2006). Cortex is driven by weak but synchronously active thalamocortical synapses. Science *312*, 1622-1627.

Chauvette, S., Crochet, S., Volgushev, M., and Timofeev I. (2011). Properties of slow oscillation during slow-wave sleep and anesthesia in cats. J. Neurosci. *31*, 14998-15008.

Contreras, D., and Steriade, M. (1995). Cellular bases of EEG slow rhythms: a study of dynamic corticothalamic relationships. J. Neurosci. *15*, 604-22.

Contreras, D., and Steriade, M. (1996). Spindle oscillation in cats: the role of corticothalamic feedback in a thalamically generated rhythm. J. Physiol. *490*, 159-179.

Contreras, D., Timofeev, I., and Steriade, M. (1996). Mechanisms of long-lasting hyperpolarizations underlying slow sleep oscillations in cat corticothalamic networks. J. Physiol. *494*, 251-264.

Contreras, D., Destexhe, A., Sejnowski, T.J., and Steriade M. (1997). Spatiotemporal patterns of spindle oscillations in cortex and thalamus. J. Neurosci. *17*, 1179-96.

Cox, C., Huguenard, J., and Prince D. (1996). Heterogeneous axonal arborizations of rat thalamic reticular neurons in the ventrobasal nucleus. J. Comp. Neurol. *366*, 416-30.

Crunelli, V., and Hughes, S.W. (2010). The slow (<1 Hz) rhythm of non-REM sleep: a dialogue between three cardinal oscillators. Nat. Neurosci. *13*, 9-17.

David, F., Schmiedt, J.T., Taylor, H.L., Orban, G., Di Giovanni, G., Uebele, V.N., Renger, J.J., Lambert, R.C., Leresche, N., and Crunelli, V. (2013). Essential thalamic contribution to slow waves of natural sleep. J. Neurosci. *33*, 19599-610.

Destexhe, A., Hughes, S.W., Rudolph, M., and Crunelli, V. (2007). Are corticothalamic “up” states fragments of wakefulness? Trends Neurosci. *30*, 334-342.

Deleuze, C., and Huguenard, J.R. (2006). Distinct Electrical and chemical connectivity maps in the thalamic reticular nucleus: potential roles in synchronization and sensation. J. Neurosci. *26*, 8633-8645.

Domich, L., Oakson, G., and Steriade, M. (1986). Thalamic burst patterns in the naturally sleeping cat: a comparison between cortically projecting and reticularis neurones. J. Physiol. *379*, 429-449.

Epzstein, J., Brecht, M., and Lee, A.K. (2011). Intracellular determinants of hippocampal CA1 place and silent cell activity in a novel environment. Neuron *70*, 109-120.

Fisher, N.I. (1993). Statistical Analysis of Circular Data (Cambridge University Press).

Gent, T., Bandarabadi, M., Herrera, C., Adamantidis, A. (2018). Thalamic dual control of sleep and wakefulness. Nat. Neurosci. 21, 974-984.

Gentet, L.J., and Ulrich, D. (2003). Strong, reliable and precise synaptic connections between thalamic relay cells and neurones of the nucleus reticularis in juvenile rats.J. Physiol. *546*, 801-11.

Groh, A., Bokor, H., Mease, R.A., Plattner, V.M., Hangya, B., Stroh, A., Deschênes, M., and Acsády, L. (2014). Convergence of cortical and sensory driver inputs on single thalamocortical cells. Cereb. Cortex *24*, 3167-3179.

Groh, A., de Kock, C.P., Wimmer, V.C., Sakmann, B., and Kuner, T. (2008). Driver or coincidence detector: modal switch of a corticothalamic giant synapse controlled by spontaneous activity and short-term depression. J. Neurosci. *28*, 9652-9663.

Halassa, M.M., Siegle, J.H., Ritt, J.T., Ting, J.T., Feng, G., and Moore, C.I. (2011). Selective optical drive of thalamic reticular nucleus generates thalamic bursts and cortical spindles. Nat. Neurosci. *14*: 1118-20.

Hirsch, J.C., Fourment, A., and Marc, M.E. (1983). Sleep related variations of membrane potential in the lateral geniculate body relay neurons of the cat. Brain Res. *259*, 308-12.

Hoogland, P.V., Wouterlood, F.G., Welker, E., and Van der Loos, H. (1991). Ultrastructure of giant and small thalamic terminals of cortical origin: a study of the projections from the barrel cortex in mice using Phaseolus vulgaris leuco-agglutinin (PHA-L). Exp. Brain Res. *87*, 159-172.

Huguenard, JR. (1996). Low-threshold calcium currents in central nervous system neurons. Annu. Rev. Physiol. *58*, 329-48.

Latchoumane, C.V., Ngo, H.V., Born, J., and Shin, H.S. (2017). Thalamic spindles promote memory formation during sleep through triple phase-locking of cortical, thalamic, and hippocampal rhythms. Neuron *95*, 424-435.

Lemieux, M., Chen, J.Y., Lonjers, P., Bazhenov, M., and Timofeev, I. (2014). The impact of cortical deafferentation on the neocortical slow oscillation. J. Neurosci. *34*, 5689-5703.

Lavallée, P., Urbain, N., Dufresne, C., Bokor, H., Acsády, L., and Deschênes, M. (2005). Feedforward inhibitory control of sensory information in higher-order thalamic nuclei. J. Neurosci. *25*, 7489-7498.

Mak-McCully, R.A., Rolland, M., Sargsyan, A., Gonzalez, C., Magnin, M., Chauvel, P., Rey, M., Bastuji, H., Halgren, E. (2017). Coordination of cortical and thalamic activity during non-REM sleep in humans. Nat Commun. *8*, 15499.

Maingret, N., Girardeau, G., Todorova, R., Goutierre, M., and Zugaro, M. (2016). Hippocampo-cortical coupling mediates memory consolidation during sleep. Nat. Neurosci. *19*, 959-64.

Matyas, F., Sreenivasan, V., Marbach, F., Wacongne, C., Barsy, B., Matéo, C., Aronoff, R., and Petersen, C.C. (2010). Motor control by sensory cortex. Science 330, 1240-43.

McCormick, D.A., and Bal, T. (1997). Sleep and arousal: thalamocortical mechanisms. Annu. Rev. Neurosci. *20*, 185-215.

Mease, R.A., Metz, M., and Groh, A. (2016a). Cortical Sensory Responses Are Enhanced by the Higher-Order Thalamus. Cell Rep. *14*, 208-15.

Mease, R.A., Sumser, A., Sakmann, B., and Groh, A. (2016b). Corticothalamic Spike Transfer via the L5B-POm Pathway in vivo. Cereb. Cortex *26*, 3461-75.

Mölle, M., Marshall, L., Gais, S., & Born, J. (2002). Grouping of spindle activity during slow oscillations in human non rapid eye movement sleep. J. Neurosci. 22, 10941-947.

Paxinos, G. and Franklin, K.B.J. (2001). The mouse brain in stereotaxic coordinates, Second Edition (Academic Press).

Pinault, D. (1996). A novel single-cell staining procedure performed in vivo under electrophysiological control: morpho-functional features of juxtacellularly labeled thalamic cells and other central neurons with biocytin or Neurobiotin. J. Neurosci. Methods *65*, 113-136.

Pinault, D., Smith, Y., and Deschênes M. (1997). Dendrodendritic and axoaxonic synapses in the thalamic reticular nucleus of the adult rat. J. Neurosci.*17*, 3215-33.

Pinault, D., and Deschênes, M. (1998). Projection and innervation patterns of individual thalamic reticular axons in the thalamus of the adult rat: a three-dimensional, graphic, and morphometric analysis. J. Comp. Neurol. *391*, 180-203.

Reichova, I., and Sherman, S.M. (2004). Somatosensory corticothalamic projections: distinguishing drivers from modulators. J. Neurophysiol. *92*, 2185-2197.

Roux, S.G., Cenier, T., Garcia, S., Litaudon, P. and Buonviso, N. (2007) A wavelet-based method for local phase extraction from a multi-frequency oscillatory signal. J. Neurosci. Methods, 160, 135-143.

Seol, M., and Kuner, T. (2015). Ionotropic glutamate receptor GluA4 and T-type calcium channel Cav3.1 subunits control key aspects of synaptic transmission at the mouse L5B-POm giant synapse. Eur. J. Neurosci. *42*, 3033-3044.

Sheroziya, M., and Timofeev, I., (2014). Global intracellular slow-wave dynamics of the thalamocortical system. J Neurosci. *34*, 8875-93.

Slézia, A., Hangya, B., Ulbert, I., and Acsády, L. (2011). Phase advancement and nucleus-specific timing of thalamocortical activity during slow cortical oscillation. J. Neurosci. *31*, 607- 617.

Steriade, M., McCormick, D.A., Sejnowski, T.J., 1993. Thalamocortical oscillations in the sleeping and aroused brain. Science *262*, 679-685.

Timofeev, I., and Steriade, M. (1996). Low-frequency rhythms in the thalamus of intact-cortex and decorticated cats. J. Neurophysiol. *76*, 4152-4168.

Urbain, N., Salin, P.A., Libourel, P.A., Comte, J.C., Gentet, L.J., and Petersen, C.C.H. (2015). Whisking-related changes in neuronal firing and membrane potential dynamics in the somatosensory thalamus of awake mice. Cell Rep. *13*, 647-656.

Veinante, P., Jacquin, M.F., and Deschênes, M. (2000). Thalamic projections from the whisker-sensitive regions of the spinal trigeminal complex in the rat. J. Comp. Neurol. *420*, 233-243.

Viaene, A.N., Petrof, I., and Sherman, S.M. (2011a). Synaptic properties of thalamic input to layers 2/3 and 4 of primary somatosensory and auditory cortices. J. Neurophysiol. *105*, 279-292.

Viaene, A.N., Petrof, I., and Sherman, S.M. (2011b). Properties of the thalamic projection from the posterior medial nucleus to primary and secondary somatosensory cortices in the mouse. Proc. Natl Acad. Sci. U.S.A. *108*, 18156-61.

Vyazovskiy, V.V., Faraguna, U., Cirelli, C., and Tononi, G. (2009). Triggering slow waves during NREM sleep in the rat by intracortical electrical stimulation: effects of sleep/wake history and background activity. J. Neurophysiol. *101*, 1921-1931.

Werth, E., Achermann, P., Dijk, D.J., and, Borbély, A.A. (1997). Spindle frequency activity in the sleep EEG: individual differences and topographic distribution. Electroencephalogr. Clin. Neurophysiol. *103*, 535-42.

Wimmer, R., Astori, S., Bond, C., Rovó, Z., Chatton, J.-Y., Adelman, J., Franken, P., and Lüthi, A. (2012). Sustaining sleep spindles through enhanced SK2-Channel activity consolidates sleep and elevates arousal threshold. J. Neurosci. *32*, 13917-928.

FIGURE LEGENDS

Figure 1 : Recording thalamic activity in awake head-restrained mice during natural sleep

(A) Schematic of experimental setup. Left, EEG and EMG electrodes were implanted, and a metal head-holder was stereotaxically glued to the skull. Right, thalamic and cortical recordings were collected together with the monitoring of the EEG and EMG.

(B) Coronal brain section counterstained with cytochrome oxidase showing the location in the VPM of the recorded cell illustrated in (C).

(C) Example VPM thalamic unit recording during a NREM episode and subsequent awakening. The NREM episode was preceded by a transitional period of drowsiness. Top to bottom: EEG and S1-LFP cortical activity, neck EMG, VPM unit activity. Both instantaneous frequency (1/interspike interval (ISI) and mean firing rate (1s bin) are represented, respectively showing that high frequency bursts of spikes could be observed specifically during NREM.

(D) Enlarged view of unit activity from the boxed area in (C) with 30ms insets showing a burst of spikes in NREM or a single spike in WK.

Figure 2 : Cortical S1-LFP is highly dynamic throughout natural NREM

(A) Top, example recordings of S1-LFP during two typical NREM episodes either followed by WK or REM (transitional intermediate state only illustrated here). Middle, corresponding S1-LFP wavelet time-frequency spectrum. Bottom, S1-LFP spindles envelope (7 - 18 Hz).

(B) Enlarged view of S1-LFP recording from the boxed area in (A), together with S1-LFP slow wave envelope (0.1 - 1.5 Hz) in light blue and detected spindles in brown.

(C) Grand average FFTs of S1-LFP computed for NREM episodes WK-f (n = 72 cells from 23 mice) or REM-f (n = 28 cells from 14 mice).

(D) Analysis of spindle features in first versus second halves of NREM episodes WK-f (n = 102) or REM-f (n = 33). Color code as in (C). Only NREM > 20 s were considered. Wilcoxon test (ratio and density analysis) or *t-test* for paired data were applied for comparison between NREM halves. Mann Whitney test (ratio and density analysis) or *t-test* for unpaired data were applied to compare data between NREM episodes.

(E) S1-LFP slow oscillations (0.1 - 1.5 Hz; n= 4584) were collected during the first (Top) and second (Bottom) halves of NREM episodes (n= 136) and phase aligned (0° corresponds to the peak of the Up-state); corresponding S1 cortical spindles were collected (n= 1845). Phase histograms were computed for, respectively, spindle onsets (black), spindle maximal amplitudes (pink) and spindle ends (blue). Arrows mark their average phases.

Figure 3 : Thalamic firing and spike timing as a function of cortical state

(A) Example VPM unit activity recorded together with S1-LFP during NREM.

(B) Enlarged view of the boxed area in (A).

(C) Mean firing rates and average burst rates of thalamic cells recorded extracellularly in second versus first half of NREM episodes, either WK-f (VPM, n= 35 cells; Pom, n= 16 cells) or REM-f (VPM, n= 13 cells; Pom, n= 8 cells). *t-test* for paired data (spike rate analysis) and Wilcoxon test (burst rate analysis) were applied to compare data between halves. *t-test* for unpaired data (spike rate analysis) and Mann Whitney test (burst rate analysis) were applied to compare data between nuclei. **, $p < 0.01$; ***, $p < 0.001$; NREM > 20s; cells considered for burst analysis if >100 spikes collected in NREM.

(D) Left, spike distribution of the cell in (A) during S1-LFP spindle cycles (10 bins / cycle). Right, spike firing preferred phases and modulation amplitudes on spindles for modulated VPM and Pom cells ($p<0.01$ Rayleigh test, n= 30 VPM cells and n= 12 Pom cells).

(E) Left, spike distribution of the cell in (A) during S1-LFP slow oscillation (0.1 - 1.5 Hz) cycles (10 bins / cycle). Right, spike firing preferred phases and modulation amplitudes on S1-LFP slow waves for modulated VPM and Pom cells ($p<0.01$ Rayleigh test, n= 32 VPM cells and n= 12 Pom cells).

(F) S1-LFP grand average (mean ± SEM) triggered on VPM (black trace) or on Pom (red trace) spikes occurring during NREM (VPM, n= 32 cells; Pom, n= 9 cells).

Figure 4 : *Delta* cortical waves and concomitant suppression of thalamic activity

(A) Top, spontaneous delta waves were detected on S1-LFP, aligned at the wave onset and a grand average wavelet time-frequency analysis was computed. Grand average PSTHs (50 ms bins) for VPM (red, n= 35 cells; n= 307 delta waves) or Pom (black, n= 19 cells; n= 155 delta waves) extracellular spike time occurrences. Corresponding grand average S1-LFP delta oscillations are overlaid.

(B) Average mean firing rates of VPM and Pom cells represented in (A).

(C) Cortical and thalamic responses to S1 light stimulation. Top, grand average of individual S1-LFP wavelet time-frequency plots following S1 light stimulation (13 cells, 20 pulses per cell). Below, Grand average S1-LFP recording (blue) and population PSTHs (10 ms bins) of thalamic response (n= 13 cells). Light blue box corresponds to 20 ms light pulse. Right: example for one cell with corresponding raster plot and overlaid S1-LFP average response.

(D) Total number of spikes (Left) and % of spikes in bursts (Right) for n= 13 VPM cells from (C) (mean ± SEM) before (baseline: -200 - 0 ms), during (0 - 20 ms) and after S1 light stimulation (from 20 to 700 ms after stimulus onset).

(E) S1-LFP and corresponding membrane potential (Vm) population averages for n= 10 VPM cells (Left) and n= 5 Pom cells (Right) aligned at spontaneous *delta* cortical waves onset.

(F) Grand average median Vm for VPM and Pom cells in (E).

(B, D, F): Data from each bin were compared to baseline using a Wilcoxon test.

Figure 5 : Membrane potential of thalamic cells across NREM

(A,B) Vm (black) recorded during a full NREM episode in a VPM (A) and a Pom (B) neurons together with S1-LFP cortical activity (blue). Red stars indicate bursts of spikes.

(C) Left, median Vm recorded during quiet wakefulness (WK) and NREM for cells recorded in both states (n= 9 VPM and 5 Pom cells). Right, median Vm recorded during the first and second parts of NREM (n= 6 VPM and 3 Pom cells; only recordings encompassing a full NREM episode were considered). Wilcoxon test was applied.

(D) Enlarged views of the red boxed areas in (A, B). Slow wave (0.1-1.5 Hz) calculated from S1-LFP (Top) and Vm (Bottom) signals are superimposed on the respective raw data (blue and red traces respectively). Red stars indicate bursts of spikes and red arrows the corresponding enlarged views on the right. Note that spikes are truncated. Boxed areas are enlarged on Figure S3.

(E) Spike distribution of VPM cells (n=6, left) and Pom cells (n=2, right) on the Vm slow oscillations (0.1 - 1.5 Hz, red trace) (10 bins / cycle).

(F) ΔVm across cortical slow waves during NREM (see STAR Methods and Figure S4). Grand averages of ΔVm (black traces) for VPM (n= 10, top) and Pom (n= 5, bottom) cells were phase-aligned on S1-LFP slow waves (0.1-1.5 Hz, blue trace) (20 bins from *-Pi* to *+Pi*). Averages of shuffled Vm and confidence intervals (±1 SD) are represented in green.

Figure 6 : Vm and S1-LFP temporal correlation

(A) S1-LFP spindle activity (blue trace) recorded concomitantly to Vm of a VPM and a Pom cells. These are enlarged views from cells illustrated in figure 5A-B (white boxes). Note that spikes are truncated.

(B) Example traces of simultaneous S1-LFP (blue) and thalamic Vm in a VPM neuron (red) exhibiting spindle oscillations. Pale blue and red rectangles indicate periods of oscillatory patterns in the 7 - 18 Hz spindle range. The percentage overlap of periods of spindle oscillations occurring in VPM Vm during total time of S1-LFP spindles (Vm on LFP), and reciprocally LFP on Vm is illustrated on the right.

(C) 7 - 18 Hz filtered traces in (B) together with cross-correlation indices between both signals calculated in 200 ms steps with a 400 ms sliding windows (purple trace). (Right) Average cross-correlation index (Right) for periods during which spindle oscillations were observed neither on S1-LFP nor VPM Vm (none), only on S1-LFP, only on VPM Vm or on both.

Figure 7 : Subthreshold activity of thalamic cells across NREM

(A-B) Example recordings of EPSPs activity during NREM from a VPM (A) and a Pom (B) cells. Spikes are truncated.

(C) Mean fast- and slow-rising EPSP rates of VPM and Pom cells (Fast-rising EPSPs, n = 10 VPM and 5 Pom cells; slow-rising EPSPs, n = 9 VPM and 5 Pom cells).

(D) Mean amplitudes of fast-rising EPSPs collected in VPM (red, n= 10) and Pom (black, n= 5) cells.

(E) Thalamic EPSPs distribution on S1-LFP spindle cycles (10 bins / cycle); a grand average per nucleus was computed (VPM, n= 9; Pom, n= 5 cells).

(F) Thalamic EPSPs distribution on S1-LFP slow oscillation cycles (0.1 - 1.5 Hz; 10 bins / cycle); a grand average per nucleus was computed (VPM, n= 9; Pom, n= 5 cells).

STAR Methods

CONTACT FOR REAGENT AND RESOURCE SHARING

Further information and requests for resources and reagents should be directed to and will be fulfilled by the Lead Contact, Nadia Urbain (nadia.urbain@inserm.fr).

EXPERIMENTAL MODEL AND SUBJECT DETAILS

All procedures were approved by the Swiss Federal Veterinary Office (authorization 1628.3) and were conducted in accordance with the European directive 86/609/EEC on the protection of animals used for experimental and scientific purposes. All efforts were made to minimize the number of animals used, as well as their stress and suffering. Experiments were carried out in male 8- to 12-week-old C57BL6J (n=20; Charles River Laboratories France) or Thy1-ChR2 mice (mice #007612, The Jackson Laboratory; n=14). After surgery, mice were housed individually to avoid deterioration of the implanted connector; they were weighted and handled daily. All animals were housed in standard conditions (23 ± 1 °C, food and water *ad libitum*) with toys to enrich their environment. All experiments were performed during the light part of the cycle (12 h light – 12 h dark).

METHOD DETAILS

Surgery for head-fixed animals

Each mouse was anesthetized with ketamine (100 mg/kg) and xylazine (8 mg/kg), and its head was positioned in a stereotaxic frame. Body temperature was monitored and maintained at 37.5°C with an electric heating pad. The skull was exposed, carefully cleaned and placed horizontally. Two stainless-steel screws were implanted over the barrel (S1) and frontal cortical areas of the right hemisphere to measure the electroencephalogram (EEG; Figure 1A). Two flexible steel wires were inserted into neck muscles for monitoring of the electromyogram (EMG). A light-weight metal head-holder, fixed to a micromanipulator fastened to the stereotaxic frame, was glued to the skull and a recording chamber implanted above the regions of interest (thalamus and S1, Figure 1B). The bone was then covered with a thin layer of acrylic cement (C&B Metabond). The metal piece was embedded in dental cement with the EEG screws and EMG wires and their four-pin connector. To prevent infection, a thin layer of cyanoacrylate glue was applied on the exposed skull before sealing the recording chamber with silicon cement (Kwik Cast, WPI, USA). An iodine solution (Betadine 10%) was applied to all the borders of the implant for subsequent healing. Twenty minutes before the end of the surgery, the mouse received a subcutaneous injection of carprofen (5 mg/kg). Ibuprofen was administered orally in the drinking water to relieve post-operative pain (50 mg Ibuprofen / 250 ml). The animal was allowed to recover from surgery and anesthesia for two days before habituation sessions began. The implant (about 1 g total weight, i.e. metal implant +

connector + cement embedding) was well-tolerated by mice, which were able to move, sleep, feed and drink normally in their home cage.

Mouse training and habituation

During two to three weeks, repetitive daily training sessions of increasing durations were performed to habituate the mice to the head-restraint. Their head was painlessly secured by screwing the metal piece, cemented to the mouse's head to a head-fixation pillar; their body lying comfortably in a cardboard roll carpeted with soft tissue. At the end of the training period, mice remained calm for several hours, during which periods of quiet wakefulness, NREM and REM sleep were typically observed.

After the training period and before the first recording session, all whiskers except for C2 were trimmed 15 mm from the skin and the location of the left C2 barrel column was functionally located through intrinsic signal optical imaging under light isoflurane anesthesia. The cortical surface was visualized through the intact bone. The C2 whisker was deflected at 10 Hz for 4 s and the evoked intrinsic optical signal was imaged by a Qicam CCD camera (Q-imaging) under 630 nm illumination provided by LEDs. The images were processed online by custom written routines running in IgorPro (Wavemetrics). A small craniotomy was then performed under isoflurane anesthesia over the functionally identified location of the C2 barrel column in order to target LFP recordings from layers 4 and 5. Another ~1 mm craniotomy was drilled over the thalamus (anteroposterior: -1.7 mm relative to Bregma; lateral: +1.0 to +1.9 mm relative to midline; Paxinos and Franklin, 2001). The dura mater was then removed and the recording chamber was closed with Kwik Cast. After four to five hours of recovery, the mouse was placed in the restraining frame as during the training sessions, and recordings were performed. In order to prevent eventual food or water deprivation during head-restraint, animals were fed regularly outside recording periods.

Surgery for anesthetized mice

Animals were prepared and surgery performed as for head-fixed animals, except that no EEG or EMG was implanted. On the day of the experiment, the location of the left C2 barrel column was functionally located through intrinsic signal optical imaging under light isoflurane anesthesia as explained above. Mice were subsequently anesthetized with ketamine (100 mg/kg) and xylazine (8 mg/kg) and their head was secured by screwing the metal piece, cemented to the mouse's head to a head-fixation pillar. Body temperature was monitored and maintained at 37.5°C with an electric heating pad. Small craniotomies were performed over the C2 barrel column and over the thalamus (as described above). The dura mater was then removed and LFP and single-unit recordings were performed. Additional anesthesia (ketamine 100 mg/kg and xylazine 2.67 mg/kg) was injected as needed intramuscularly (every 45 - 60 minutes).

Single-unit and polygraphic recordings

Single-units in the thalamus were recorded with glass micropipettes lowered vertically (50 - 80 MOhms) filled with a solution of potassium acetate (1M) and Neurobiotin (1.5%, Vector Laboratories, Burlingame, CA). Signals were amplified and low-pass filtered (3 kHz; AxoClamp 2B, Axon Instruments), fed to an oscilloscope and an audio monitor, and digitized at 20 kHz. Thalamic recordings were collected together with LFP recordings (MultiClamp 700A; band-pass filtered 0.1 - 300 Hz) in layer 4 or 5 of the S1 C2 column, performed with glass micropipettes lowered with a 45° angle (5-7 µm) filled with a solution of sodium chloride (0.15 M), and with amplified EEG (band-pass filtered 0.1 - 300 Hz) and EMG (band-pass filtered 30 - 300 Hz) polygraphic signals (P55 Grass Instruments) (Figure 1B). The reference electrode for recordings with glass micropipettes was located on the surface of the skull, inside the recording chamber filled with sterile saline solution. All signals were collected via an ITC-18 analog-to-digital converter (Instrutech) using AxoGraph software (AxoGraph Scientific, Sydney, Australia).

Initial localization of thalamic cells was based on the coordinates described in Paxinos and Franklin (2001). Manual deflection of individual contralateral (right side) whiskers was performed in order to determine the receptive field of the extracellularly recorded cells. The remaining 15mm of the trimmed whiskers were sufficient to manually stimulate each of them individually in our setup. Cell locations were determined by the intracellular or juxtacellular labeling of the last recorded unit (Pinault, 1996; 27 cells, n = 34 mice) and the reconstruction of each pipette track. A Pom / VPM boundary line was extrapolated for each mouse, the cells located within an area of 100 µm above and 100 µm below this line was considered as "boundary" cells (n = 21), and were not pooled with either VPM or Pom cells. All cells assigned to the VPM and tested for whisker deflections (39/43 of VPM cells recorded extracellularly and 9/22 of VPM cells recorded intracellularly) were mono- or multi-whisker responsive cells, while only 3 out of 22 Pom tested cells displayed any clear response to whisker deflections.

At the end of experiments, mice were perfused under deep anesthesia with saline, followed by a fixative containing 4 % paraformaldehyde in phosphate buffer (PB 0.1 M, pH 7.4). Brains were post-fixed for 30 minutes, and coronal slices were subsequently cut at 70 µm-thickness with a vibratome. Sections were processed for cytochrome oxidase and Neurobiotin histochemistry according to standard protocols (Veinante et al., 2000).

QUANTIFICATION AND STATISTICAL ANALYSIS

Cortical and behavioral states

The activity of thalamic cells was recorded together with EEG and LFP in the ipsilateral S1 (C2 column) either in layer 4 (450-550 µm depth) or in layer 5 (600-700 µm depth). In addition, the muscle tone was monitored from the neck (EMG) and whisker movements were tracked with a high-speed camera. All these parameters allowed us to determine the vigilance state of the mouse. In this paper, we focus on thalamic activity and its relationship with cortical states specifically during non-REM sleep (NREM). NREM was distinguished by high-amplitude, low frequency EEG

(0.5-3 Hz) and LFP (0.1-1.5 Hz) activity (see figures 2C, S1A) with a strong dominant frequency range of 7-18 Hz (spindle activity, see figure 2A-C), associated with a weak EMG tone. Transitional and intermediate states (such as drowsiness, transition from NREM to REM sleep, see figures 1C, 2A) were excluded from the analysis. Importantly, NREM is a different state from Quiet wakefulness (see Urbain et al., 2015): both cortical LFP and EEG spectra are clearly distinct in NREM and in the Quiet state, with a strong dominant frequency range of 2-8 Hz in the S1-LFP in the latter state (Figure S1B). NREM is also clearly distinguishable from REM sleep, since REM sleep is characterized by cortical EEG spectra with a strong dominant *theta* band (~ 8 Hz) and no muscle tone at EMG.

Spike time occurrences were determined as threshold amplitude crossings (threshold was set to 7-12 SD of the background noise). The spike detection was checked (and corrected if necessary) for each NREM episodes included in the analyses.

Burst detection and burst analysis

Raw data were imported into Matlab for analysis using custom-written functions. Bursts were defined as two or more spikes that were preceded by at least 65 ms of silence and had interspike intervals (ISIs) < 8 ms. A maximal ISI of 8 ms was chosen preferentially to the most conservative 4 ms ISI (Lu et al., 1992), in order to include the last spikes fired in long bursts (see figure S2). Only cells for which > 100 spikes were collected during NREM were considered for this study. No ISI < 1ms was observed, indicating single-unit recording (see figure S2A,B). In order to illustrate the high frequency bursts activity during a whole NREM episode, we showed on Figure 1C the instantaneous frequency of the thalamic cell, calculated as 1/interspike interval (ISI), together with the mean firing rate (1s bin).

Phase analysis

During NREM episodes, S1-LFP slow wave was obtained by filtering the S1-LFP signal in the 0.1 - 1.5 Hz frequency band (signal was first downsampled at 100Hz and we then applied an order 3 Butterworth forward-backward filter). The slow wave was considered to be continuous during the whole NREM episode. The phase of action potentials (APs) relative to *slow oscillation* cycles in the S1-LFP was determined by the angle of the instantaneous phase (derived from a Hilbert transformation of the filtered S1-LFP) at the location of spikes (Slézia et al., 2011). The trough of the slow wave was defined as 0° and the peak as 180°. These two points define the reference frame, which enables us to compare waves with different shapes and lengths. Phase histogram, mean angle and mean vector length were calculated using circular statistical methods for each recording (Fisher, 1993). Only neurons that fired at least 100 action potentials during the appropriate NREM segments were included to ensure statistically reliable estimates of firing phases.

S1-LFP spindles were observed as transient oscillatory events in the 7 - 18 Hz frequency range. They were detected by applying a ridge line detection on the wavelet time frequency map (Figure 2A, Morlet wavelet, f_0=1.5, for further details see Roux et al., 2007). The threshold for spindle detection was set as 4 times the median power of the 7-18Hz band excluding NREM periods. Only oscillations spanning more than 3 cycles were kept for analysis. Occasionally, two putative spindles could be detected at the same time but distinct frequencies. Careful analysis of these cases led to define a partial selection criterion: for strong overlap (more than 50% of the duration of the low frequency putative spindle) the low frequency putative spindle was kept only if its average power during the overlap exceeded the average power of the high frequency putative spindle in the same period by more than 50%. Otherwise, the low frequency putative spindle was eliminated (4.2 % of total detected spindles). Finally, for short overlap, both putative spindles were kept for future analysis. Each detected spindle was converted into a time frequency line giving for each time point: instantaneous frequency, phase and power of the spindle. Phase of detected troughs in S1-LFP was defined as 0°. For each cell, we built phase histograms of spike timing relative to spindle troughs, and firing was considered to be modulated by the oscillations if $p<0.01$ using the Rayleigh test. Only neurons that fired at least 100 action potentials during spindle oscillations were included to ensure statistically reliable estimates of firing phase.

Level and phase of coupling with respectively *slow* or spindle oscillations were assessed for each modulated cell by averaging unit vectors at each AP phase from all *slow* or spindle oscillation cycles (see figure 3 E-F). Only neurons with significant phase coupling to spindles were processed further ($p<0.01$, Rayleigh's test, Slézia et al., 2011). Ten out of the 43 VPM cells (23%) were C2-responding cells. Since we did not observe any difference in thalamocortical relations relative to the barreloid location of the thalamic neurons, data were pooled for modulated cells.

Delta events were detected by visual inspection for each cell, aligned at the wave onset; a wavelet time-frequency analysis of S1-LFP was computed and corresponding thalamic spike time occurrences were distributed in a Peristimulus Time Histogram (-250 to + 750 ms PSTH, 50 ms bins, see figure 4A). Only VPM and Pom cells which exhibited more than 10 spikes during this 1s-time window were considered for analysis.

Frequency spectra

To compute the FFT of EEG and cortical LFP, 4 seconds epochs during stable NREM (episodes > 16 sec) were selected and averaged across 78 cells recorded from 21 mice. Both EEG and S1-LFP signals were downsampled to 512 Hz and the offset removed before FFT computation with a 0.5 Hz bin size. When several epochs of NREM were collected, data were averaged to obtain one FFT per cell, for both the EEG and S1-LFP. In the case of S1-LFP, a grand average per layer was first calculated, but since no differences appeared between data collected for L4 and L5, the data across layers were pooled. From EEG and S1-LFP FFTs, the *theta* (5 - 11 Hz) / *delta* (1 - 4Hz) amplitude ratios were computed.

Spike-triggered averaging (STA)

Thalamic spikes were collected for cells exhibiting more than 100 spikes in NREM to trigger S1-LFP averages. Only spikes occurring more than 65 ms after the previous spike were considered (i.e. min ISI = 65 ms). These spikes triggered the S1-LFP collection from -0.1 s to 0.2 s ("0 s" = spike time). S1-LFPs were collected and averaged (n = 231.8 ± 30.4 spikes per cell; range: 104 - 1075 spikes per cell) per cell. Grand averages per layer were first calculated. Since no difference appeared between data collected for the L4 and L5, data were pooled for both layers.

Thalamic membrane potential dynamics in NREM

Only high-quality sharp intracellular recordings with little or no current injection were taken into account (under anesthesia, I=0 nA for the 12 recorded cells; non-anesthetized mice, I=0 nA for 14 out of 15 cells and -0.3 nA applied in one cell). Cells included in the following analysis exhibited >50 mV amplitude and <0.6 ms half-width spontaneous or evoked spikes (in case of silent cells). If the AP half-width increased by more than 15%, the subsequent data were excluded from further analysis. To quantify thalamic membrane potentials (V_m), the median V_m was considered, and not the mean, in order to mitigate spike contribution.

Spontaneous EPSPs, > 3.5 SD of the "noise", were detected using the template-matching algorithm built into AxoGraph and visually inspected. The EPSP mean rate was computed by counting the number of EPSPs and dividing by the time spent in NREM. Note that since only EPSPs > 3.5 SD of the "noise" were collected, EPSP mean rate is inevitably underestimated for all cells. For the characterization of EPSP features, we analyzed only isolated EPSPs, or the first EPSP in a burst of EPSPs. All EPSPs were averaged for a given cell, then a grand average was calculated. EPSP amplitude was measured from baseline to the peak and the 20-80% rise time was determined. Previously, we described two populations of EPSPs for thalamic cells by plotting for all isolated EPSPs their amplitudes as a function of their rise times (Urbain et al., 2015). Therefore, EPSPs were separated according to their rise time values into fast-rising EPSPs (20-80% rise time < 0.5 ms and < 0.6 ms for VPM and Pom cells respectively) and slow-rising EPSPs (20-80% rise time > 0.5 ms and > 0.6 ms for VPM and Pom cells respectively).

Cross-correlation analysis of Vm-S1-LFP

Cross-correlations between both signals were performed using the function cross-correlation for continuous signals of Neuroexplorer (Plexon). Vm and S1-LFP signals were first downsampled to 512 Hz and then low pass filtered at 50 Hz. An average of cross-correlation for all NREM bouts was calculated for each VPM cell and then a grand average was computed for all cells.

For the purpose of computing changes in cross-correlations between thalamic Vm and cortical S1-LFP through NREM episodes (Figure 6), a 400ms sliding window in steps of 200ms was applied to the 7-18Hz filtered Vm and LFP traces and the absolute peak of the cross-

correlations was registered in a time window ranging from -10 ms to +10 ms (Figure 6C). Second, start and end times of spindle oscillations were computed for both Vm and S1-LFP and rounded to the nearest 200ms. The averages of peak cross-correlations in and out of spindle oscillations were then computed for both Vm and S1-LFP and for epochs during which spindle oscillations were observed in both or neither traces.

Vm slow wave was obtained by filtering the Vm signal in the 0.1 - 1.5 Hz frequency band (signal was first downsampled at 100Hz and we then applied an order 3 Butterworth forward-backward filter). The slow wave was considered to be continuous during the whole NREM episode. The phase of action potentials (APs) relative to the Vm slow oscillation cycles was determined by the angle of the instantaneous phase (derived from a Hilbert transformation of the filtered Vm) at the location of spikes. The trough of Vm slow wave was defined as 0° and the peak as 180°. These two points define the reference frame, which enables us to compare waves with different shapes and lengths. Phase histogram, mean angle and mean vector length were calculated using circular statistical methods for each recording.

For Vm averages using phase of S1-LFP slow oscillation as a reference, S1-LFP slow waves were collected and divided in 20 bins from *-Pi* to *+Pi* radians (or equivalently -180° to 180°). Corresponding Vm were collected and averaged per bin across S1-LFP cycles (n = 14.4 ± 5.6, range: 6 to 32 cycles). To compute the grand average, mean Vm was substracted from Vm oscillation to remove variability due to changes in resting membrane potential. In addition, for each thalamic cell, we shuffled the Vm averages (same Vm values but randomly distributed across cycle bins) and computed the phase histograms between shuffled unit Vm and S1-LFP cycles. Statistics and associated confidence intervals were based on 1000 iterations. To assess the statistical significance of Vm oscillation average, we compared the amplitude of the average oscillation (obtained with a sinusoidal fit) with the amplitude distribution of the shuffled Vm. The p-value was then obtained by looking at the rank of the real oscillation amplitude in the distribution of shuffled oscillation amplitudes.

All VPM cells (n= 10) recorded intracellularly were recorded in the area responding to the row C whiskers, for 2 of them we were able to identify that they were precisely recorded in the C2 barreloid area. We did not observe any difference in the relations to cortical activity of these two latter cells compared with the other 8 VPM cells. Therefore, data were pooled in population analysis.

Spike and EPSP phase-locking analysis

The distribution of fast-rising EPSPs on S1-LFP cortical slow (0.1 - 1.5 Hz) and spindle oscillations was calculated for cells where more than 10 EPSPs were collected in NREM.

The distribution of thalamic intracellular spikes on thalamic-Vm slow oscillations (0.1 - 1.5 Hz) was calculated for cells where more than 5 spikes were collected in NREM. The phases of action potentials / EPSPs relative to slow or spindle oscillations in the S1-LFP (or thalamic-Vm)

were determined using the same method as for the distribution of thalamic extracellular spikes described above in the part "*Phase analysis, spikes timing of thalamic cells on the cortical waves"*.

Optogenetic stimulation

Optogenetic experiments were performed on Thy1-ChR2 mice expressing the channelrhodospin ChR2-YFP fusion protein in layer 5 cortical neurons; these layer 5 neurons are accessible for photoactivation *in vivo* due to the extensive ChR2-YFP expression in apical dendrites at the surface of the brain (Arenkiel et al., 2007). Light pulses were delivered via a 470 nm LED coupled with a 500 µm diameter core optical fiber positioned above S1 cortex. For each cell, 20 pulses of 20 ms duration at 0.8 Hz were applied. Intensity of 1.5 - 3.5 mW/mm^2 was applied in order to evoke cortical response without inducing noticeable behavioral response. Further analysis of whisker movements filmed with a high-speed camera revealed that activation of S1 cortex drove short-latency small whisker retractions, in accordance with Matyas et al. (2010).

Statistical analysis

Data analysis was performed using AxoGraph, Spike2, Matlab, IgorPro, Python, OriginPro and Excel software. Unless otherwise stated, results are reported as mean ± SEM. Basic statistical analysis was performed using Statview. The Bonferroni/Dunn test was chosen when a post hoc test was applied. Circular statistics was performed using Python and Oriana (Kovach Computing Services software). Statistical tests are specified in the figure legends. The numbers of cells and mice considered for each test are provided in the main text or / and in figure legends. Additional statistical measures (such as mean, median, range) are provided in Tables S1 and S2. Significance levels *: $p < 0.05$; **: $p < 0.01$; ***: $p < 0.001$.

For the analyses were NREM episodes were segregated in two parts, first and second halves, only NREM episodes with start (i.e. transition from waking) and end (i.e. transition to wakefulness or REM sleep) were considered.

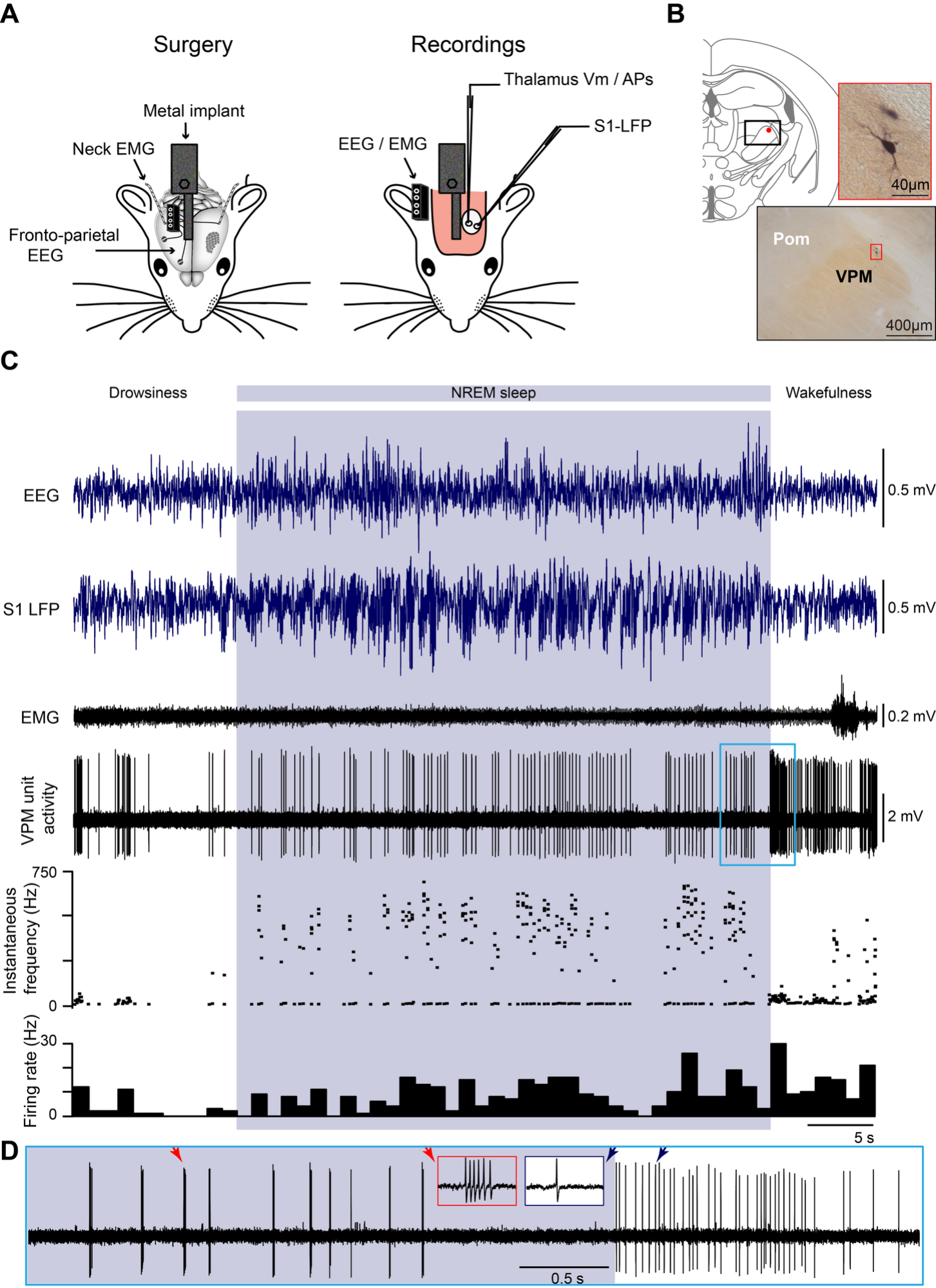
A
Surgery
Recordings
Metal implant
Neck EMG
Fronto-parietal EEG
Thalamus Vm / APs
S1-LFP
EEG / EMG
B
40µm
Pom
VPM
400µm
C
Drowsiness
NREM sleep
Wakefulness
EEG
0.5 mV
S1 LFP
0.5 mV
EMG
0.2 mV
VPM unit activity
2 mV
Instantaneous frequency (Hz)
750
0
Firing rate (Hz)
30
0
5 s
D
0.5 s

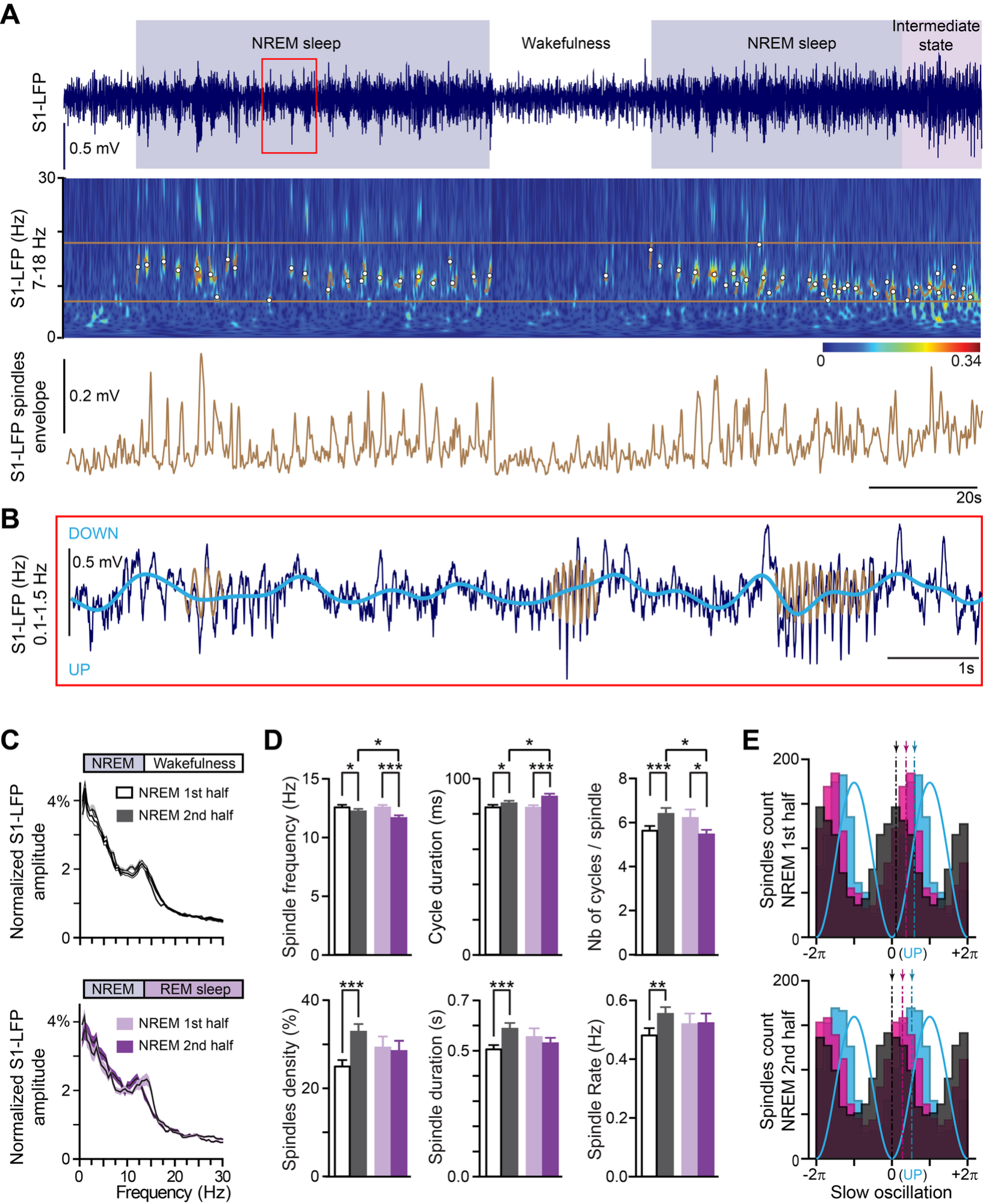
A
NREM sleep
Wakefulness
NREM sleep
Intermediate state
S1-LFP
0.5 mV
30
S1-LFP (Hz)
7-18 Hz
0
0
0.34
S1-LFP spindles envelope
0.2 mV
20s
B
DOWN
0.5 mV
S1-LFP (Hz)
0.1-1.5 Hz
UP
1s
C
NREM
Wakefulness
NREM 1st half
NREM 2nd half
4%
Normalized S1-LFP amplitude
2
0
NREM
REM sleep
NREM 1st half
NREM 2nd half
4%
Normalized S1-LFP amplitude
2
0
0
10
20
30
Frequency (Hz)
D
Spindle frequency (Hz)
15
10
5
0
Cycle duration (ms)
100
0
Nb of cycles / spindle
8
6
4
2
0
Spindles density (%)
40
20
0
Spindle duration (s)
0.7
0.5
0.0
Spindle Rate (Hz)
0.6
0.4
0.2
0.0
E
Spindles count NREM 1st half
200
0
-2π
0 (UP)
+2π
Spindles count NREM 2nd half
200
0
-2π
0 (UP)
+2π
Slow oscillation

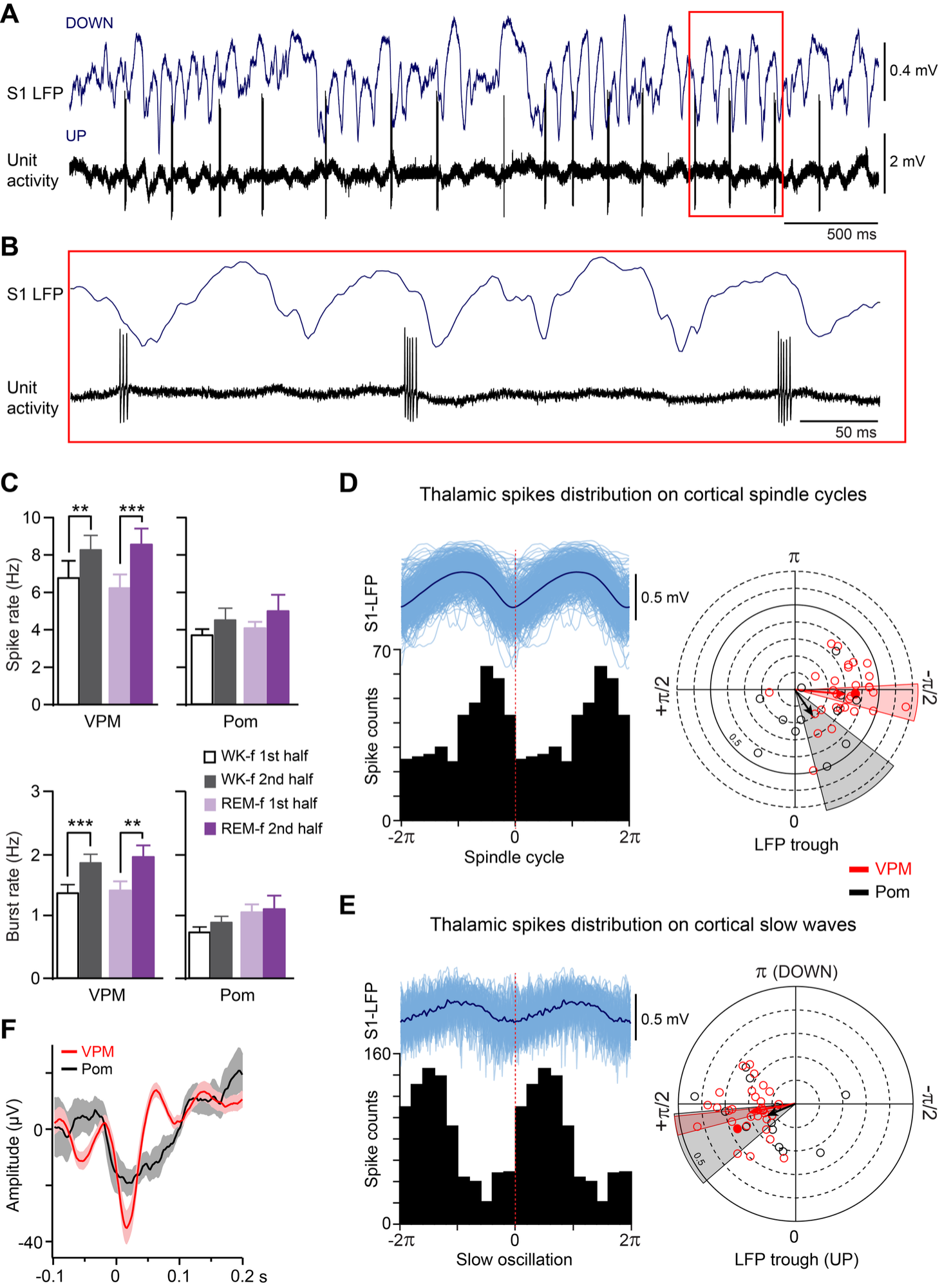
A
DOWN
S1 LFP
UP
Unit activity
0.4 mV
2 mV
500 ms
B
S1 LFP
Unit activity
50 ms
C
Spike rate (Hz)
VPM
Pom
WK-f 1st half
WK-f 2nd half
REM-f 1st half
REM-f 2nd half
Burst rate (Hz)
D
Thalamic spikes distribution on cortical spindle cycles
S1-LFP
0.5 mV
Spike counts
Spindle cycle
LFP trough
VPM
Pom
E
Thalamic spikes distribution on cortical slow waves
Slow oscillation
LFP trough (UP)
F
Amplitude (μV)
0.2 s

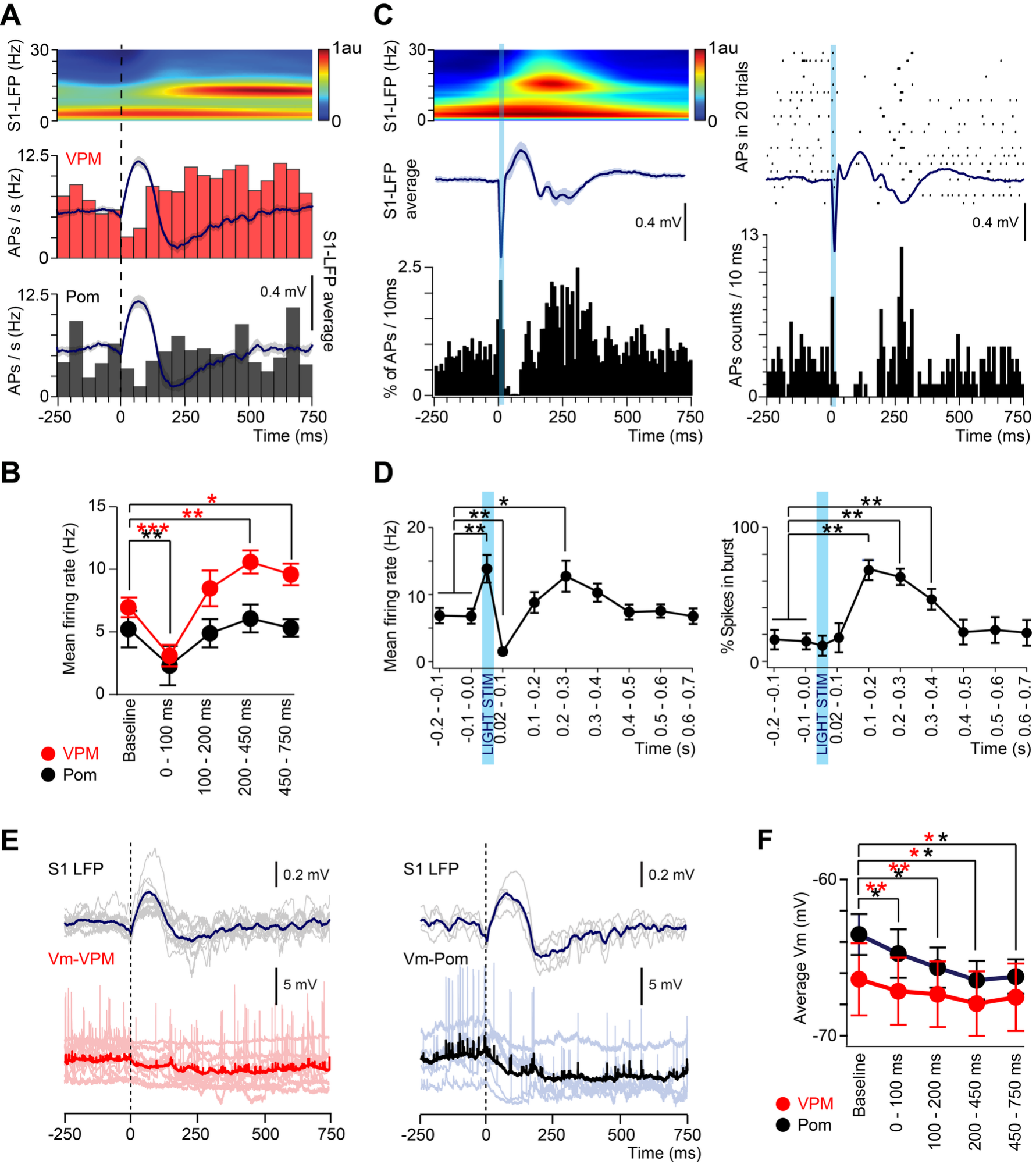
A
S1-LFP (Hz)
30
0
1au
0
VPM
12.5
APs / s (Hz)
0
S1-LFP average
Pom
0.4 mV
-250
0
250
500
750
Time (ms)
C
S1-LFP average
0.4 mV
% of APs / 10ms
2.5
APs in 20 trials
APs counts / 10 ms
13
B
Mean firing rate (Hz)
15
10
5
Baseline
0 - 100 ms
100 - 200 ms
200 - 450 ms
450 - 750 ms
VPM
Pom
D
LIGHT STIM
Time (s)
% Spikes in burst
100
E
S1 LFP
0.2 mV
Vm-VPM
5 mV
Vm-Pom
F
Average Vm (mV)
-60
-70

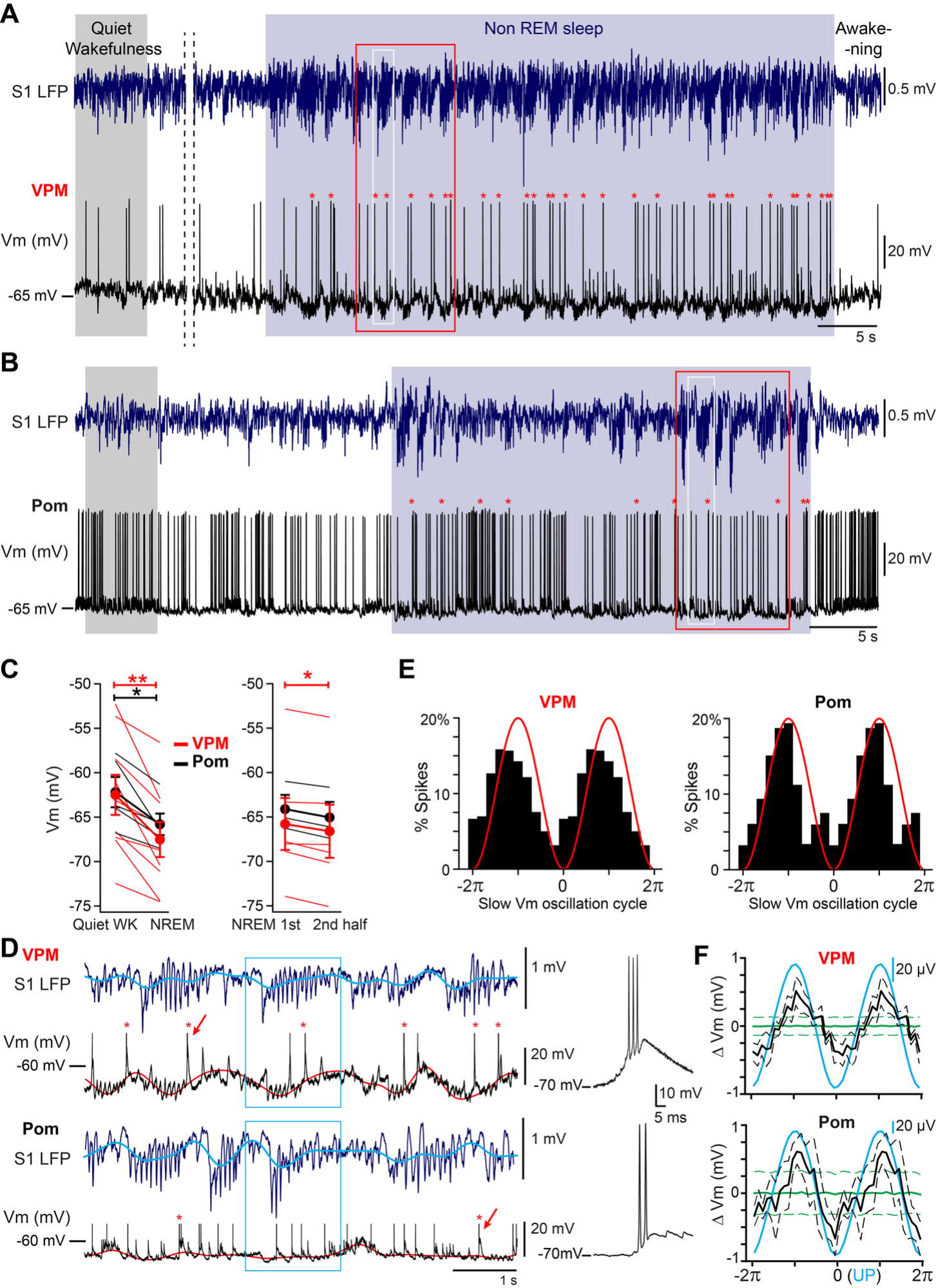
A
Quiet Wakefulness
Non REM sleep
Awake--ning
S1 LFP
0.5 mV
VPM
Vm (mV)
20 mV
-65 mV
5 s
B
S1 LFP
0.5 mV
Pom
Vm (mV)
20 mV
-65 mV
5 s
C
Vm (mV)
VPM
Pom
Quiet WK
NREM
NREM 1st
2nd half
D
VPM
S1 LFP
1 mV
Vm (mV)
-60 mV
20 mV
-70 mV
10 mV
5 ms
Pom
S1 LFP
1 mV
Vm (mV)
-60 mV
20 mV
-70mV
1 s
E
VPM
Pom
% Spikes
Slow Vm oscillation cycle
F
VPM
Pom
Δ Vm (mV)
20 μV
0 (UP)

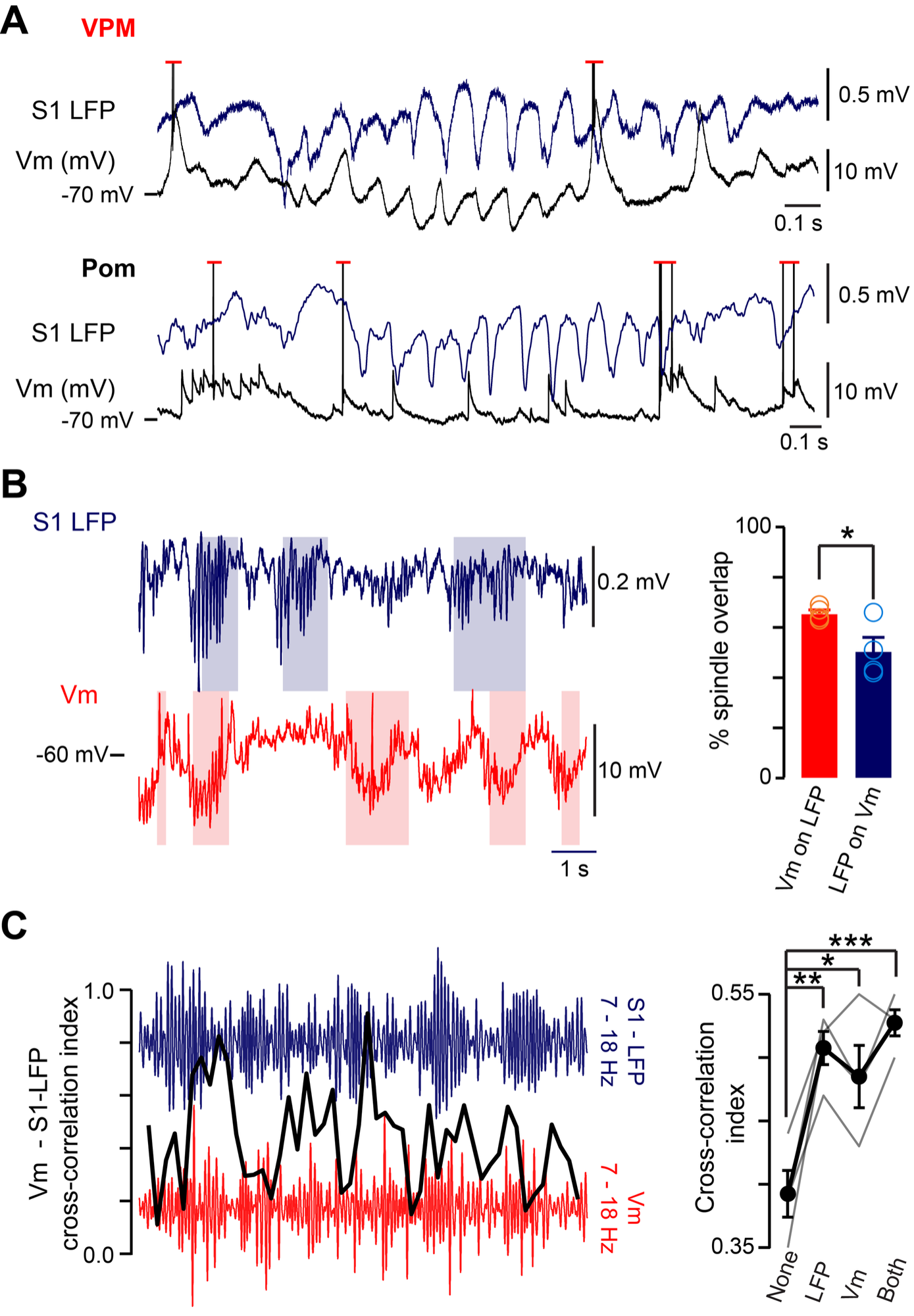
A
VPM
S1 LFP
Vm (mV)
-70 mV
0.5 mV
10 mV
0.1 s
Pom
S1 LFP
Vm (mV)
-70 mV
0.5 mV
10 mV
0.1 s
B
S1 LFP
0.2 mV
Vm
-60 mV
10 mV
1 s
100
0
% spindle overlap
*
Vm on LFP
LFP on Vm
C
Vm - S1-LFP
cross-correlation index
1.0
0.0
S1 - LFP
7 - 18 Hz
Vm
7 - 18 Hz
***
*
**
0.55
0.35
Cross-correlation
index
None
LFP
Vm
Both

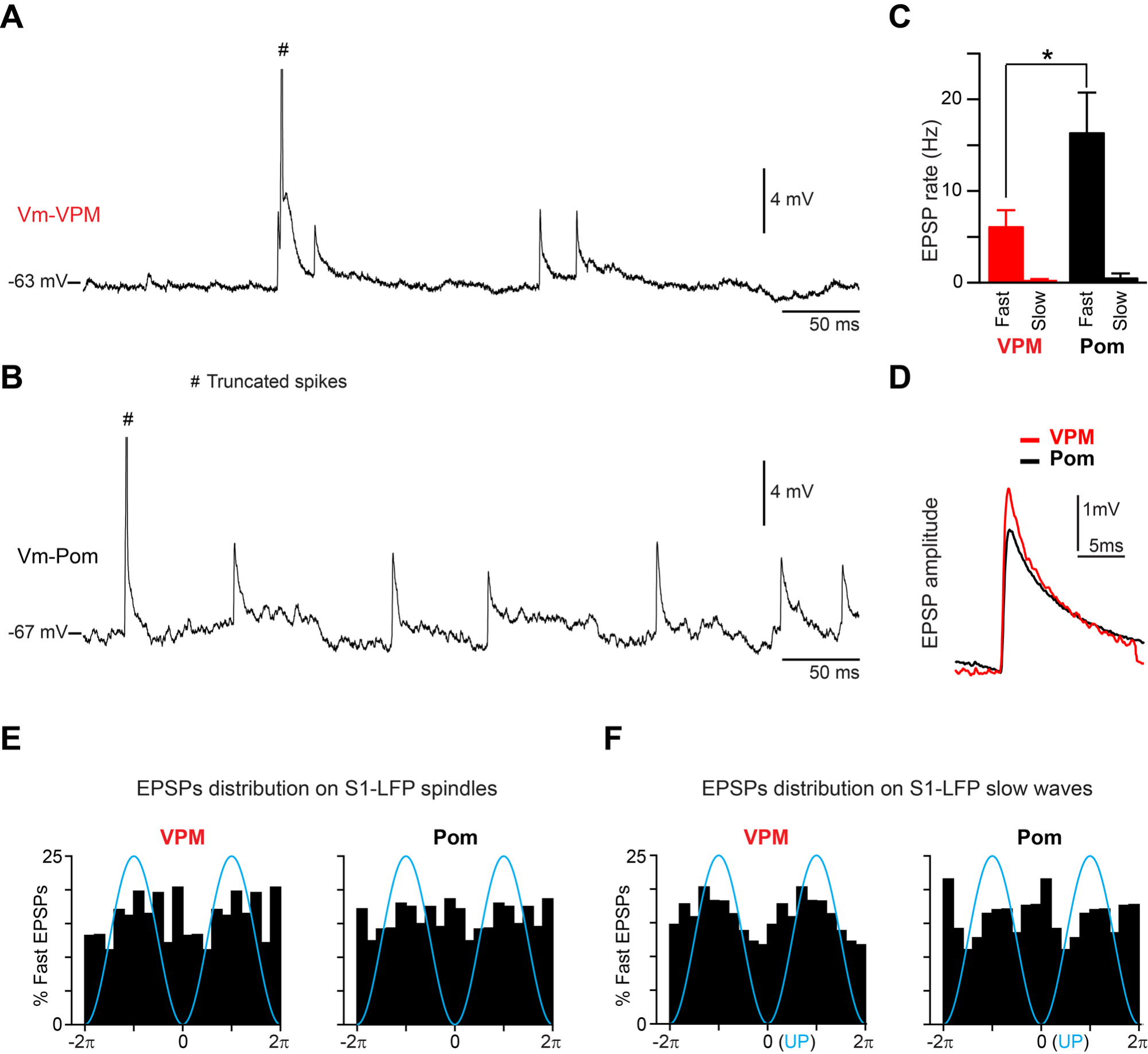
A
#
Vm-VPM
4 mV
-63 mV
50 ms
B
Truncated spikes
#
4 mV
Vm-Pom
-67 mV
50 ms
C
*
EPSP rate (Hz)
20
10
0
Fast
Slow
Fast
Slow
VPM
Pom
D
VPM
Pom
EPSP amplitude
1mV
5ms
E
EPSPs distribution on S1-LFP spindles
VPM
Pom
% Fast EPSPs
25
0
-2π
0
2π
F
EPSPs distribution on S1-LFP slow waves
VPM
Pom
% Fast EPSPs
25
0
-2π
0 (UP)
2π

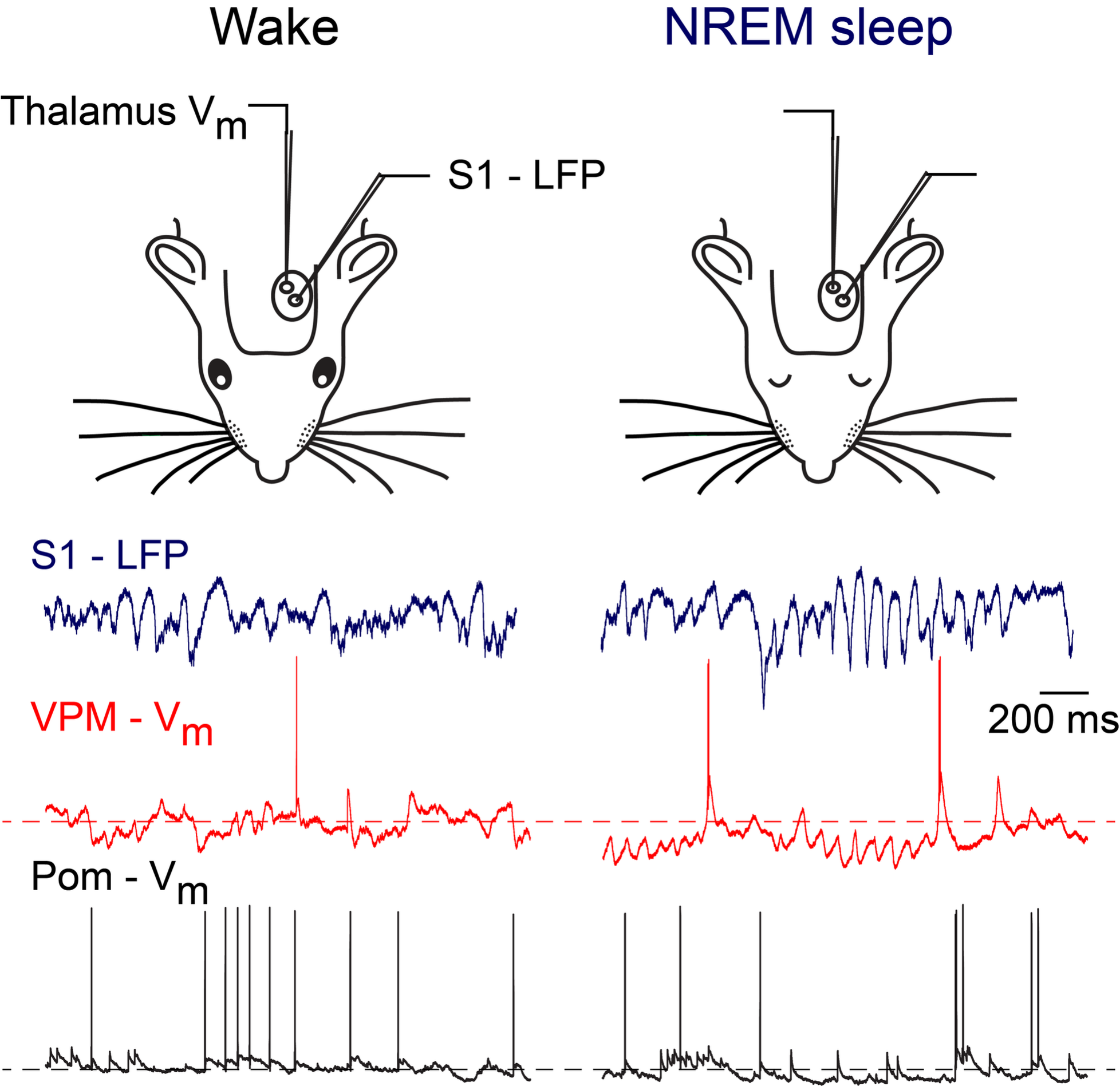
Wake
NREM sleep
Thalamus V_m
S1 - LFP
S1 - LFP
VPM - V_m
Pom - V_m
200 ms